Advances in Water Resources 111 (2018) 239–258

Contents lists available at ScienceDirect

Advances in Water Resources

journal homepage: www.elsevier.com/locate/advwatres

# Benchmarks for single-phase flow in fractured porous media

Bernd Flemisch[*,a], Inga Berre[b], Wietse Boon[b], Alessio Fumagalli[b], Nicolas Schwenck[a], Anna Scotti[c], Ivar Stefansson[b], Alexandru Tatomir[d]

[a] Department of Hydromechanics and Modelling of Hydrosystems, University of Stuttgart, Pfaffenwaldring 61, Stuttgart 70569, Germany
[b] Department of Mathematics, University of Bergen, Allégaten 41, Bergen 5007, Norway
[c] Laboratory for Modeling and Scientific Computing MOX, Politecnico di Milano, p.za Leonardo da Vinci 32, Milano 20133, Italy
[d] Department of Applied Geology, Geosciences Center, University of Göttingen, Goldschmidtstrasse 3, Göttingen 37077, Germany

ARTICLE INFO

*Keywords:*
Fractured porous media
Discretization methods
Benchmark

ABSTRACT

This paper presents several test cases intended to be benchmarks for numerical schemes for single-phase fluid flow in fractured porous media. A number of solution strategies are compared, including a vertex and two cell-centred finite volume methods, a non-conforming embedded discrete fracture model, a primal and a dual extended finite element formulation, and a mortar discrete fracture model. The proposed benchmarks test the schemes by increasing the difficulties in terms of network geometry, e.g. intersecting fractures, and physical parameters, e.g. low and high fracture-matrix permeability ratio as well as heterogeneous fracture permeabilities. For each problem, the results presented are the number of unknowns, the approximation errors in the porous matrix and in the fractures with respect to a reference solution, and the sparsity and condition number of the discretized linear system. All data and meshes used in this study are publicly available for further comparisons.

## 1. Introduction

In porous-media flow applications, the domains of interest often contain geometrically anisotropic inclusions and strongly discontinuous material coefficients that can span several orders of magnitude. If the size of these heterogeneities is small in normal direction compared to the tangential directions, these features are called fractures. Fractures can act both as conduits and barriers and affect flow patterns severely. Target applications concerning fractured porous-media systems in earth sciences include groundwater resource management, renewable energy storage, recovery of petroleum resources, radioactive waste reposition, coal bed methane migration in mines, and geothermal energy production.

The analysis and prediction of flow in fractured porous media systems are important for all the aforementioned applications. Many different conceptual and numerical models of flow in fractured porous-media systems can be found in the literature. Even though fractured porous-media systems have been of interest to modelers for a long time, they still present challenges for simulators. During the last 70 years, different modeling approaches have been developed and gradually improved. Comprehensive reviews can be found in Berkowitz (2002), Dietrich et al. (2005), Hoteit and Firoozabadi (2008), Neumann (2005), Sahimi (2011) and Singhal and Gupta (2010). Roughly, the fractured porous media systems are classified in two broad categories: discrete fracture-matrix (DFM) models and continuum fracture models. Within this paper, we will only consider DFM models.

The DFM models consider flow occurring in both the fracture network and the surrounding rock matrix. They account explicitly for the effects of individual fractures on the fluid flow. An efficient way to represent fractures in DFMs is the hybrid-dimensional approach, see e.g. Helmig (1997), Flauraud et al. (2003), Bogdanov et al. (2003), Firoozabadi and Monteagudo (2004), Karimi-Fard et al. (2004), Martin et al. (2005) and Reichenberger et al. (2006). Fractures in the geometrical domain are then discretized with elements of co-dimension one with respect to the dimension of the surrounding matrix, such as one-dimensional elements in two-dimensional settings. Due to the similarities in these models, the gradient scheme framework (Brenner et al., 2016; 2017) allows for a unified analysis of a number of DFM models. The aforementioned classical DFM approaches all rely on matching fracture and matrix grids in the sense that a fracture element coincides geometrically with co-dimension-one mesh entities, i.e. faces of matrix grid elements. In addition to the classical models, several so-called non-conforming DFM models have been developed in recent years, such as EDFM (Hajibeygi et al., 2011; Moinfar et al., 2014), XFEM-based approaches (D'Angelo and Scotti, 2012; Huang et al., 2011; Schwenck et al., 2015), or mortar-type methods (Frih et al., 2012).

* Corresponding author.
*E-mail address:* bernd.flemisch@iws.uni-stuttgart.de (B. Flemisch).

https://doi.org/10.1016/j.advwatres.2017.10.036
Received 5 January 2017; Received in revised form 27 October 2017; Accepted 30 October 2017
Available online 31 October 2017
0309-1708/ © 2017 Elsevier Ltd. All rights reserved.

Benchmarking represents a methodology for verifying, testing and comparing the modeling tools. Various codes have been developed by academic institutions or companies based on different conceptual, mathematical, and numerical models. Even though benchmarking studies are increasing in all fields of engineering and workshops have been organized around specific problems (e.g. Class et al., 2009), there are still only a limited number of studies. Some are related to a specific application and are flexible as to how the problem is modeled in terms of assumptions regarding the physics and the selection of the domain, see Class et al. (2009), Nordbotten et al. (2012), Caers (2013) and Kolditz et al. (2015). Others De Dreuzy et al. (2013) and Caers (2013), like ours, focus on the comparison of numerical schemes.

One of the common requirements when selecting the test problems for comparing numerical schemes is that they allow the examination of the capabilities of each of the compared methods. Therefore, our benchmark study proposes a set of problems starting from simple geometries and then gradually increasing the geometrical complexity. The test problems are specifically selected to make clear distinctions between the different methods. They consist of existing and new computational benchmarks for fluid flow in fractured porous media and allow for comparison of several DFM-based numerical schemes in a systematic way.

We would like to invite the scientific community to follow up on this study and evaluate further methods by means of the proposed benchmarks. In order to facilitate this, the paper is accompanied by grid and result files in the form of a Git repository at https://git.iws.uni-stuttgart.de/benchmarks/fracture-flow.

The remainder of this paper is organized as follows. In Section 2, we formulate the model problem in terms of the partial differential equation to be solved. The participating DFM models are described in Section 3. The central Section 4 proposes the benchmarks and compares the results of the different methods. Finally, Section 5 concludes with a summary and outlook.

## 2. The model problem

We consider an incompressible single-phase flow through a porous medium, assumed to be described by Darcy's law, resulting in the governing system of equations

$$\mathbf{u} = -\mathbb{K}\,\mathbf{grad}\,p, \tag{1a}$$

$$div\,\mathbf{u} = q, \tag{1b}$$

in an open bounded domain $\mathscr{D} \subset \mathbb{R}^N$, subject to boundary conditions

$$p = p_{\mathrm{D}} \quad \text{on } \partial\mathscr{D}_{\mathrm{D}}, \tag{1c}$$

$$\mathbf{u}\cdot\mathbf{n} = q_{\mathrm{N}} \quad \text{on } \partial\mathscr{D}_{\mathrm{N}}, \tag{1d}$$

with $\partial\mathscr{D} = \overline{\partial\mathscr{D}_{\mathrm{D}} \cup \partial\mathscr{D}_{\mathrm{N}}}$ and $\partial\mathscr{D}_{\mathrm{D}} \cap \partial\mathscr{D}_{\mathrm{N}} = \emptyset$. In Eq. (1) $\mathbf{u}$ denotes the macroscopic fluid velocity whereas $\mathbb{K}$ and $p$ stand for absolute permeability and pressure.

Let us assume that $\mathscr{D}$ contains several fractures, that all together constitute a single domain $\Gamma$ of spatial dimension $N$ such that $\Gamma \subset \mathscr{D}$, which is a possibly unconnected, open subset of $\mathscr{D}$. The surrounding porous rock, namely, the remaining part of $\mathscr{D}$, is called $\Omega = \mathscr{D} \setminus \overline{\Gamma}$. Assuming that the fracture aperture $\varepsilon$ at each point of $\Gamma$ is small compared to other characteristic dimensions of the fractures, the full-dimensional domain $\Gamma$ can be reduced to the $(N-1)$-dimensional fracture network $\gamma$. This reduction involves modeling choices resulting in different hybrid-dimensional problem formulations that form the basis for the methods presented in the following section.

## 3. Participating discretization methods

Within this section, the discretization methods participating in this benchmark study are described. The purpose of this article is the comparison of well-known, established and/or at least published methods. Therefore, only the most significant aspects of each method are summarized. We do not show a comparison against analytical solutions here. The analysis of the methods and theoretical results such as proofs of optimal convergence can be found in the corresponding references. A summary of all participating methods is provided in Table 1. In the sequel, we will denote with *d.o.f.* the degrees of freedom associated to a specific method. We indicate also the type of conformity required to the computational grid with respect to the fractures and the assumption that the pressure is considered continuous across the fractures. With the exception of P-XFEM, all considered methods are locally conservative by construction.

**Table 1**
Participating discretization methods.

| Method | d.o.f. | frac-dim | conforming | *p*-cont |
|---|---|---|---|---|
| Box | $p$ (vert) | dim-1 | yes | yes |
| TPFA | $p$ (elem) | dim-1 | yes | no |
| MPFA | $p$ (elem) | dim-1 | yes | no |
| EDFM | $p$ (elem) | dim-1 | no | yes |
| Flux-Mortar | $p$ (elem), $\boldsymbol{u}$ (faces) | dim-1 | geometrically | no |
| P-XFEM | $p$ (vert) | dim-1 | no | no |
| D-XFEM | $p$ (elem), $\boldsymbol{u}$ (faces) | dim-1 | no | no |
| MFD | $p$ (faces) | dim | geometrically | no |

The lower-dimensional representation of fractures allows for easier mesh generation for both conforming and non-conforming methods in comparison to the equi-dimensional approach, as it circumvents the appearance of very small elements when discretizing the interior of the fracture (i.e., within the fracture width). Conform meshing implies that the fractures are discretized with a set of line elements (in a 2D domain) that are also the edges of the triangular finite elements.

### 3.1. Vertex-centred, continuous-pressure, conforming lower-dimensional DFM (Box)

The Box method is a vertex-centred finite-volume method proposed in e.g. Helmig (1997) which combines the advantages of finite element and finite volume grids, allowing unstructured grids and guaranteeing a locally conservative scheme (Reichenberger et al., 2006). Fig. 1 illustrates a two-dimensional representation of the dual-grid with two finite elements $E_1$ and $E_5$ sharing the same edge $(ij_1)$ that represents a lower-dimensional fracture with the aperture $\varepsilon_{ij_1}$. The main characteristic in terms of the fractured system is that the pressure is required to be continuous, in particular in those vertices whose control volumes overlap both fracture and matrix regions.

The Box method used for this paper is implemented in the open-source numerical simulator DuMu$^{\mathrm{x}}$. A detailed description of the conceptual, mathematical and numerical model and code implementation is published in Tatomir (2012). The simulation code used for the benchmark studies is publicly available under https://git.iws.uni-stuttgart.de/dumux-pub/Flemisch2016a.git.

### 3.2. Cell-centred, discontinuous-pressure, conforming DFM (TPFA)

The control volume finite difference method uses a two-point flux approximation (TPFA) based on the cell-centre pressure values for the evaluation of the face fluxes. The method is a widely applied and standard method for simulation of flow in porous media. The domain is partitioned with fractures coinciding with the interior faces between matrix cells just as described at the beginning of Section 3. The flux over the face between matrix cells $i$ and $j$ is approximated by

$$\mathbf{u}_{ij} = T_{ij}(p_i - p_j), \tag{2}$$

where $p_i$ and $p_j$ are the pressures in the neighbouring cells and $T_{ij}$ is the face transmissibility, computed as the harmonic average of the two half

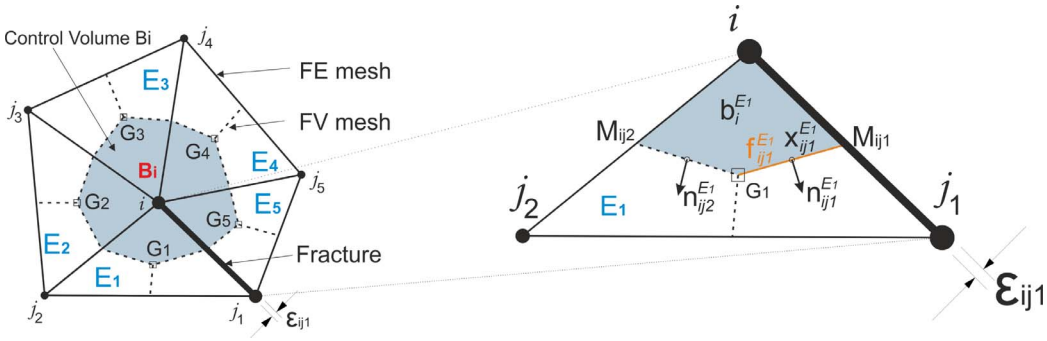


**Fig. 1.** Conceptual representation of the Box method: (left-hand side) The dual finite element and finite volume mesh from which the control volume $B_i$ around node $i$ is created. Node $i$ is surrounded by nodes $\{j_1, j_2, j_3, j_4, j_5\}$, where segment $ij_1$ represents both a fracture and a shared FE edge; (right-hand side) Sub-control volume (SCV) $b_i^{E_1}$ in element $E_1$ has barycentre $G_1$ and the mid-points of the edges $ij_1$ and $ij_2$ are $M_{ij1}$, respectively $M_{ij2}$. The SCV face $f_{ij1}^{E1}$ is the segment $\overline{G_1 M_{ij1}}$ which contains the integration point $x_{ij1}^{E1}$ where the normal vector $\mathbf{n}_{ij1}^{E1}$ is applied.

transmissibilities corresponding to the face and the two cells. The half transmissibility of cell-face pair $i$ is in turn given as

$$\alpha_i = \frac{A_i \mathbf{n}_i^{\top} \mathbb{K}_i}{\mathbf{d}_i^{\top} \mathbf{d}_i} \cdot \mathbf{d}_i, \tag{3}$$

where $A_i$ and $\mathbf{n}_i$ are the area and unit normal vector of the face, $\mathbb{K}_i$ is the permeability assigned to the cell and $\mathbf{d}_i$ is the distance vector from cell centre to face centroid.

In addition to the unknowns given at the centroids of the matrix cells, unknowns are associated to the centroids of the fracture cells. The fracture cells are associated with apertures, which multiplied with the length give the volume of these cells. The aperture is also used to construct hybrid faces for the matrix-fracture interfaces. These faces, parallel to the fracture but displaced half an aperture to either side, enable us to compute the half transmissibilities between the fracture cell and the matrix cells on the two sides. These faces are indicated by the dashed blue lines in Fig. 2, where the computational domain is superimposed on the geometrical grid. The result is a hybrid grid with fractures which are lower dimensional in the grid, but equi-dimensional in the computational domain at the cost of a small matrix volume error corresponding to the overlap of the matrix cells with the fracture cells.

Following the method proposed by Karimi-Fard et al. (2004), the intermediate fracture intersection cell drawn with dashed red lines in Fig. 2 is removed, leading to direct coupling of the fracture cells neighbour to the intersection. The purpose of this is both to obtain a smaller condition number and to avoid severe time-step restrictions associated with small cells in transport simulations. To each new face between cell $i$ and $j$, face transmissibilities are assigned, calculated using the star delta transformation as described in Karimi-Fard et al. (2004):

$$T_{ij} = \frac{\alpha_i \alpha_j}{\sum_{k=1}^{n} \alpha_k}, \tag{4}$$

with $n$ denoting the number of fracture cells meeting at the intersection.

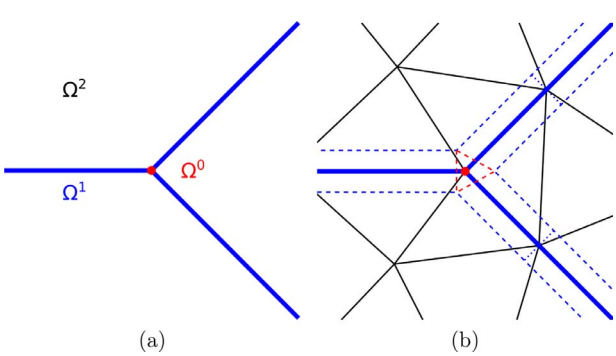


**Fig. 2.** (a) Conceptual decomposition of the domain according to element dimension with the matrix depicted in black, fractures in blue and their intersections in red. (b) The computational domain of the TPFA method. Dashed lines are faces of the fracture cells. (For interpretation of the references to colour in this figure legend, the reader is referred to the web version of this article.)

As this elimination disregards all information on the permeability of the intersection, it should be used with caution in cases of crossing fractures of different permeability. We encounter this feature in Section 4.3, and include results both with and without the elimination for one of the test cases presented in that section.

### 3.3. Cell-centred, discontinuous-pressure, conforming DFM (MPFA)

Inspired by the TPFA method presented above, a method based on the multi-point flux approximation has been developed (Sandve et al., 2012), see also e.g. Ahmed et al. (2015). The MPFA variant of the method reduces errors associated with the TPFA approach for grids that are not close to K-orthogonal, and avoids errors related to the splitting of the fluxes in the star-delta transformation. The method is constructed letting each face flux depend on the pressures of several of the neighbouring cells. Specifically, an interaction region defined by cell centroids and continuity points at the faces around each node is constructed (see Fig. 3) and the pressure is assumed to be linear within each cell of the region. Intermediate pressure unknowns are introduced at the continuity points and express the flux over each half face in terms of the weighted pressures of all cell centre and continuity point pressures of the region. Continuity of the flux over each face allows for elimination of the continuity point pressures and a relationship between flux and pressure of the form

$$\mathbf{u}_i = \mathbb{T}_i \mathbf{p} \tag{5}$$

for each half face $i$ is obtained. Here, $\mathbf{p}$ denotes the pressures at the cell centres of the interaction region and $\mathbb{T}_i$ accounts for the effect of geometry and permeability of those same cells. For a detailed description of the method, see, e.g., Aavatsmark (2002).

The handling of the fractures is similar to the one described for the TPFA. For the fracture intersections, the pressure is assumed to be

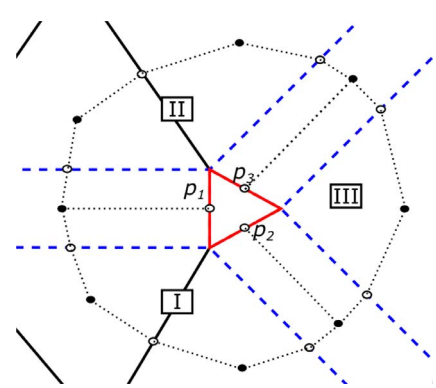


**Fig. 3.** The three interaction regions (dotted lines) around one fracture intersection for the MPFA consisting of four (I and II) and three (III) sub cells each. The continuity points are marked by circles and the cell centres by black dots. Fracture-matrix faces are depicted by blue dashed lines and the intermediate intersection cell in red. Figure adapted from Sandve et al. (2012). (For interpretation of the references to colour in this figure legend, the reader is referred to the web version of this article.)

constant within the intersection and continuous over the hybrid faces. After elimination of the intermediate pressures ($p_1$, $p_2$ and $p_3$ in Fig. 3), there are no unknowns directly associated to the intersection cells and these are removed from the computational grid. The Eq. (5) type equations are assembled for each cell and the resulting linear system solved for the cell centre pressures.

We refer to Sandve et al. (2012) for a thorough comparison of the TPFA and MPFA approaches. The implementations of both methods are available in the open-source Matlab Reservoir Simulation Toolbox, http://www.sintef.no/projectweb/mrst/ (Lie et al., 2012). An extension of control volume methods to non-matching grids across fractures may be found in Tunc et al. (2012).

### 3.4. Continuous-pressure, non-conforming embedded DFM (EDFM)

Recently, non-conforming methods for the treatment of lower-dimensional fractures have been developed, for example in Moinfar et al. (2011); 2014) and Hajibeygi et al. (2011), to avoid the time-consuming construction of complex matrix grids which explicitly represent the fractures. They are mostly used in the context of single and multi-phase flow simulations for petroleum engineering applications and require the normal fracture permeability to be orders of magnitude higher than the matrix permeability, as in the case of fractured petroleum reservoirs. In this field of applications corner-point grids are normally employed to describe the geological layers, e.g. different rock type, of the reservoir. An adaptation of such computational grids to the fractures could be unaffordable for real cases. The numerical method belongs to the family of two-point schemes, where a one-to-one connection between the degrees of freedom is considered through the transmissibility concept (Eymard et al., 2000). References on the embedded discrete fracture method (EDFM) can be found, for example, in Li and Lee (2008), Panfili et al. (2013), Moinfar et al. (2014), Panfili and Cominelli (2014), de Araujo Cavalcante Filho et al. (2015) and Fumagalli et al. (2016).

In practice, the mesh of the fractures is generated on top of the rock grid so that each rock cell cut by fractures contains exactly one fracture cell per fracture. Intersections between fractures are computed without affecting the creation of the grids of fractures and rock and used to compute approximate transmissibilities between different fracture cells. See Fig. 4 as an example. A degree of freedom that represents a pressure or a saturation value is assigned to each matrix cell and to each fracture cell. This means that transmissibilities between matrix and fracture cells, as well as those between different fracture cells, need to be computed. We compute the transmissibility between a fracture cell and a matrix cell $T_{fm}$ and the half-transmissibility $T_i$ between two

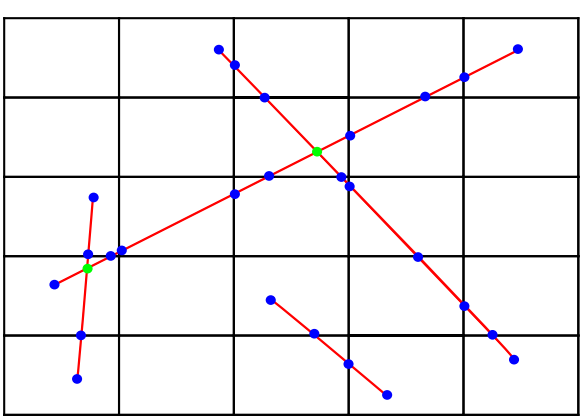

**Fig. 4.** Example of meshes, for both fractures and rock matrix, suited for EDFM. The rock matrix is considered as a background mesh. Each fracture cell is represented by two blue dots and the green dots are the non-matching intersection among fractures. (For interpretation of the references to colour in this figure legend, the reader is referred to the web version of this article.)

intersecting fracture cells (related to the fracture $i$) through the following approximate expressions:

$$T_{fm} = A\frac{\mathbf{n}_f^{\mathsf{T}}\mathbb{K}\cdot\mathbf{n}_f}{d_{f,m}} \quad \text{and} \quad T_i = s\frac{k_i\varepsilon_i}{d_{i,s}}.$$

Here $A$ is the measure of the fracture cell in the current rock cell, $\mathbf{n}_f$ is the normal of the fracture cell and $d_{f,\,m}$ is an average distance between the fracture cell and the matrix cell, see Li and Lee (2008). For the fracture-fracture transmissibility, $s$ indicates the measure of the intersecting segment, $k_i$ the scalar permeability of the fracture, $\varepsilon_i$ the aperture and $d_{i,\,s}$ is the average distance between the fracture cell and the intersecting segment. The standard harmonic average is considered to compute the transmissibility between the two fracture cells. Standard formulae for fracture-fracture as well as matrix-matrix transmissibilities are computed by means of a two-point flux approximation. It is worth to notice that the recent extension of EDFM called Projection-based EDFM (pEDFM), proposed in Tene et al. (2017), is also able to handle low permeable fractures. Finally, even if the proposed benchmark cases are two-dimensional the method can be extended to three dimensions without any additional constraints.

### 3.5. Cell-centred, discontinuous-pressure, geometrically-conforming mortar DFM (Flux-Mortar)

The key concept behind the Flux-Mortar, as described more thoroughly in Boon et al. (2016), is the idea that fractures can be considered as interfaces between different sub-domains. This has been explored previously by Martin et al. (2005) and Frih et al. (2012), among others. In this context, we consider the domain decomposition technique known as the mortar method to model flow through the fractured porous medium.

The mortar method is generally used to couple equations in different sub-domains by introducing a so-called mortar variable, defined on the interface. In case of modeling fracture flow, a well-explored choice of the mortar variable is the fracture pressure (Martin et al., 2005). The method considered here, however, uses the flux between matrix and fracture domains as the mortar variable, which leads to a stronger imposition of mass conservation. One of the main advantages of the close relationship to mortar methods is the capability to handle non-matching grids. In particular, two sub-domains bordering a fracture can be meshed independently on both sides, as illustrated in Fig. 5. The difficulty in mesh generation is then relieved significantly since only the geometry of the fractures needs to be respected.

By construction, the Flux-Mortar is applicable to problems in arbitrary dimensions. The governing equations in the matrix and the fractures (as well as fracture intersections in 3D) are identical and thus all fractures, intersections and tips are handled in a unified manner. Consequently, although only two-dimensional problems are considered in this study, the discretization scheme also applies to problems in three dimensions.

Due to a slightly different derivation of the reduced model, the scheme handles spatially varying apertures. Moreover, the apertures may be arbitrarily close, or even equal to zero which naturally eliminates the possibility of flow in the tangential direction.

With the use of mixed finite elements, mass is conserved locally in the matrix, fractures, and fracture intersections. The flux $\mathbf{u}$ in the matrix and fractures are modeled using the lowest-order Raviart–Thomas elements and linear Lagrange elements, respectively. The pressure $p$ is then given by piecewise constants in the matrix, as well as the fractures and intersection points. Additionally, the mortar variable is given by piecewise constants on a separately generated, lower-dimensional, mortar grid on the matrix-fracture interface. This grid matches with the surrounding grids in case of matching grids and is coarser otherwise.

The resulting mixed finite element formulation is a saddle-point problem, which may be challenging to solve numerically. To relieve

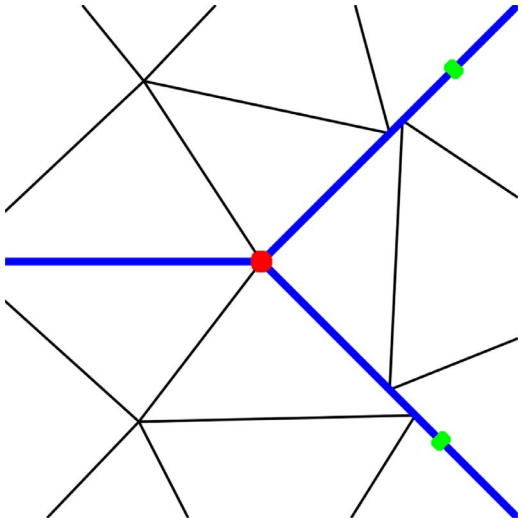

**Fig. 5.** The Flux-Mortar method allows for non-matching grids along fracture interfaces. Fracture and matrix flows are coupled using a mortar variable, defined on a coarser grid (green dots). (For interpretation of the references to colour in this figure legend, the reader is referred to the web version of this article.)

this, the flux variables may be eliminated through hybridization, which leads to a less computationally expensive scheme containing solely the cell-centre pressures.

Two implementations of the method have been developed, both of which are used in this benchmark study. The first version, implemented in MATLAB, is suited for simpler geometries in 2D, containing relatively few fractures, such as those considered in Benchmarks 1–3. The second version has been implemented for 3D problems and higher-order spaces on matching grids using the open-source finite element library FEniCS (Logg et al., 2012). This code is more efficient for complex cases such as Benchmark 4.

### 3.6. Discontinuous-pressure, non-conforming primal XFEM (P-XFEM)

The primal XFEM method participating in this benchmarking study is described in detail in Schwenck (2015), see also Flemisch et al. (2016) and Schwenck et al. (2015). The method is based on the hybrid-dimensional problem formulation investigated in Martin et al. (2005), where conditions for the coupling between fracture and matrix are derived:

$$\{\mathbf{u}_{\mathrm{m}}\cdot\mathbf{n}\}_\gamma = k_{\mathrm{f,n}}/\varepsilon[[p_{\mathrm{m}}]]_\gamma \tag{6a}$$

$$\xi_0[[\mathbf{u}_{\mathrm{m}}\cdot\mathbf{n}]]_\gamma = k_{\mathrm{f,n}}/\varepsilon\left(\{p_{\mathrm{m}}\}_\gamma - p_{\mathrm{f}}\right) \tag{6b}$$

Here, the subscripts “m” and “f” indicate matrix and fracture quantities, while $\{\{\cdot\}\}_\gamma$ and $[[\cdot]]_\gamma$ denote the average and the jump of a matrix quantity over the fracture $\gamma$, respectively.

The coupling conditions (6) can be used to define a source term for the fracture flow problem, while they yield an interface problem for the matrix domain. For the discretization of this interface problem, the methodology presented in Hansbo and Hansbo (2002) is used, which amounts to applying the eXtended Finite Element Method (XFEM). Together with an independent standard discretization of the lower-dimensional fracture problem, this yields a hybrid-dimensional, non-conforming primal XFEM-based method. The XFEM space is built enriching the standard Lagrangian $\mathbb{P}_1$ (or $\mathbb{Q}_1$ for quads) finite-element spaces, whose degrees of freedom are located at the vertices of the full-dimensional grid of the matrix $\Omega$ and the lower-dimensional grid of the fracture $\gamma$. A representative example of matrix and fracture grids is illustrated in Fig. 6. Unlike the EDFM method, see Fig. 4, the fracture grid

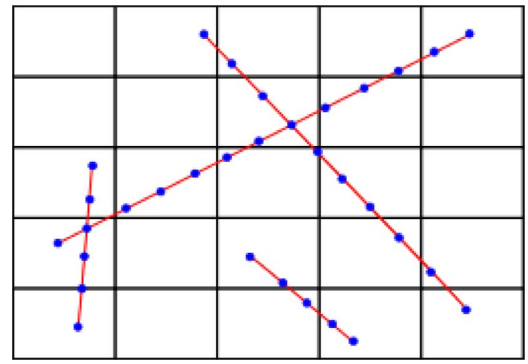

**Fig. 6.** Example of meshes, for both fractures and rock matrix, suited for P-XFEM. The fracture grid vertices are indicated by the blue dots. (For interpretation of the references to colour in this figure legend, the reader is referred to the web version of this article.)

vertices can be placed arbitrarily without taking into account the matrix grid. On the other hand, the method requires matching fracture branch grids in the form of vertices placed at the fracture intersections. In particular, special care has to be taken of intersecting and immersed fractures (Schwenck et al., 2015).

The method is implemented on top of the DUNE framework (Bastian et al., 2008) and the discretization module DUNe-PDELab (Bastian et al., 2010). For the enrichment of the finite-element spaces in the context of XFEM, the modules DUNe-Multidomain and DUNe-Multidomaingrid are employed (Müthing, 2015). The simulation code for the XFEM approach and for the benchmarks studied here is publicly available under https://git.iws.uni-stuttgart.de/dumux-pub/Flemisch2016a.git. Currently, the method is only implemented in 2D. Conceptually, no difficulties arise for extending it to 3D. However, the possibly multiple enrichment of the function spaces for matrix elements intersected by fracture elements can become a very tedious task for complex fracture networks.

### 3.7. Discontinuous-pressure, non-conforming dual XFEM (D-XFEM)

The dual XFEM method participating in his benchmark is based on D’Angelo and Scotti (2012). The method, originally derived for a domain cut by one fracture, was further developed in Formaggia et al. (2014) and Fumagalli and Scotti (2014) to account for intersecting fractures with different permeabilities. The same equations and coupling conditions as for the primal XFEM are used, but in a dual formulation where Darcy law and mass conservation give rise to a saddle-point problem for the fluid mean velocity and pressure, both in the fracture and in the surrounding medium. Moreover, unlike the previous method, this method employs triangular/tetrahedral grids. The usual lowest order $\mathbb{RT}_0 - \mathbb{P}_0$ pair for velocity and pressure is enriched following (Hansbo and Hansbo, 2002) in the elements of the porous medium cut by a fracture, or in the elements of a fracture at the intersection with other fractures. Indeed, triangular/tetrahedral grids are arbitrarily cut by triangulated lines/surfaces in 2D and 3D respectively. These surfaces can, in turn, intersect each other in a non-conforming way, as shown in Fig. 7.

In the current implementation of the method no special enrichment is added in the bulk elements containing the fracture tips. Instead, fractures are artificially extended up to the boundary of the domain, and in the extension we prescribe the same permeability of the surrounding porous medium to obtain a “virtual” fracture with no effects on the flow.

The method has been implemented on the basis of the Getfem++ library, http://download.gna.org/getfem/html/homepage/ , which provides support for the computation of the intersections and the quadrature on sub-elements thanks to an interface with QHull, http://www.qhull.org/.

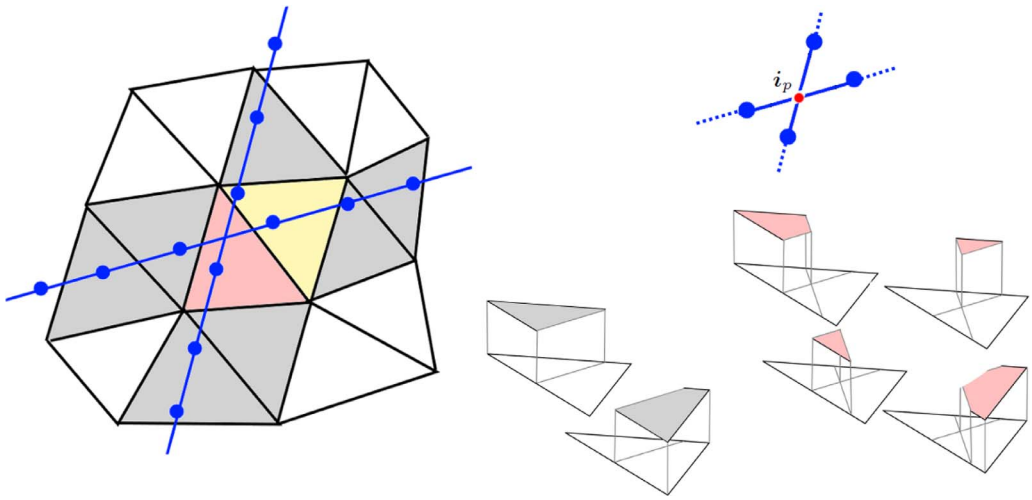


**Fig. 7.** A portion of the grid cut by two fractures: in the two dimensional case they can split the elements in two (grey), three (yellow), or four (red) independent parts, where the restrictions of the basis functions are defined. The fracture grids are irrespective of the bulk grid and of each other, i.e. the intersection point $i_p$ is not a point of the grid. (For interpretation of the references to colour in this figure legend, the reader is referred to the web version of this article.)

### 3.8. Reference solutions calculated with mimetic finite differences (MFD)

The reference solutions are computed on very fine grids that discretize both matrix and fractures by full-dimensional triangular or quadrilateral elements. A mimetic finite difference method, see Brezzi et al. (2005) and Flemisch and Helmig (2008), is used to discretize problem (1). The method is employed as it is implemented in DuMu$^{x}$ 2.7 (Flemisch et al., 2011). In particular, a mixed-hybrid approach is used to transform the discrete saddle point problem in terms of cell pressures and face fluxes into a symmetric positive definite formulation with face-pressure degrees of freedom.

## 4. Benchmark problems

This is the main section, which compares the methods described above by means of four benchmark cases. The first benchmark case, considered in Section 4.1, is based on Geiger et al. (2013) and shows a regular fracture network. Second, in Section 4.2, we present a well established benchmark for groundwater flow from Swedish Nuclear Power Inspectorate (SKI) (1987) that contains two crossing, highly permeable fractures and a non-straight top surface. After that, a small but complex fracture network exhibiting immersed fractures and intersections at different angles is investigated in Section 4.3. Finally, a case synthesized from a real application is considered in Section 4.4.

For each benchmark case, a description of the computational domain is provided, including boundary conditions, the geometrical information about the corresponding fracture network and the associated material parameters such as aperture and permeability. For some of the cases, the reference solution on the complete domain is visualized. This is followed by illustrations of the grids used by the participating methods. Since the methods pose different grid requirements, the grid could be chosen arbitrarily for each method, provided that the number of grid cells or vertices is roughly the same. If a reference solution is available (Benchmarks 1–3), the results of the different methods are compared by evaluating the errors with respect to the reference in the matrix domain as well as in the fracture network, indicated by $err_{\mathrm{m}}$ and $err_{\mathrm{f}}$, respectively. The errors are calculated according to the formulas

$$err_{\mathrm{m}}^2 = \frac{1}{|\Omega|(\Delta p_{\mathrm{ref}})^2} \sum_{f=K_{\mathrm{ref,m}}\cap K_{\mathrm{m}}} |f| \left( p_{\mathrm{m}}|_{K_{\mathrm{m}}} - p_{\mathrm{ref}}|_{K_{\mathrm{ref,m}}} \right)^2, \tag{7a}$$

$$err_{\mathrm{f}}^2 = \frac{1}{|\gamma|(\Delta p_{\mathrm{ref}})^2} \sum_{e=K_{\mathrm{ref,f}}\cap K_{\mathrm{f}}} |e| \left( p_{\mathrm{f}}|_{K_{\mathrm{f}}} - p_{\mathrm{ref}}|_{K_{\mathrm{ref,f}}} \right)^2, \tag{7b}$$

where $|\Omega|$ and $|\gamma|$ indicate the size of the full-dimensional matrix and the lower-dimensional fracture domain, respectively, and $\Delta p_{\mathrm{ref}} = \max_{\mathscr{D}} p_{\mathrm{ref}} - \min_{\mathscr{D}} p_{\mathrm{ref}}$. The sum is taken over all intersections of (full-dimensional) elements $K_{\mathrm{ref,\ m}}$ and $K_{\mathrm{ref,\ f}}$ of the grid employed for the reference solution with full-dimensional matrix elements $K_{\mathrm{m}}$ in case of $err_{\mathrm{m}}$ and lower-dimensional fracture elements $K_{\mathrm{f}}$ in case of $err_{\mathrm{f}}$. The quantities $|f|$ and $|e|$ indicate the area of a full-dimensional intersection $f$ and a lower-dimensional intersection $e$, respectively. We stress the fact that for the calculation of the matrix error $err_{\mathrm{m}}$, only elements $K_{\mathrm{ref,\ m}}$ in the matrix part of the equi-dimensional grid are considered. In other words, the full-dimensional fracture domain $\Gamma$ is excluded from this calculation. In addition to errors in matrix and fracture, the densities and condition numbers of the resulting linear system matrices are provided. Moreover, a comparison is performed by means of plots along specific lines through the domain for some benchmark cases. Each case is concluded by a short discussion of the results.

### 4.1. Benchmark 1: regular fracture network

This test case is based on an article presenting a new dual continuum model, Geiger et al. (2013), with slightly modified boundary conditions and material properties. The computational domain including the fracture network and boundary conditions is shown in Fig. 8. The matrix permeability is set to $\mathbb{K}_{\mathrm{m}} = \mathbb{I}$, all fractures have a uniform aperture $\varepsilon = 10^{-4}$. For the fracture permeability we consider two cases: a highly conductive network with $k_{\mathrm{f,n}} = k_{\mathrm{f,t}} = 10^4$, as worked out in Section 4.1.1, and a case with blocking fractures by setting $k_{\mathrm{f,n}} = k_{\mathrm{f,t}} = 10^{-4}$, as described in Section 4.1.2. The reference solutions are computed on a grid which resolves every fracture with 10

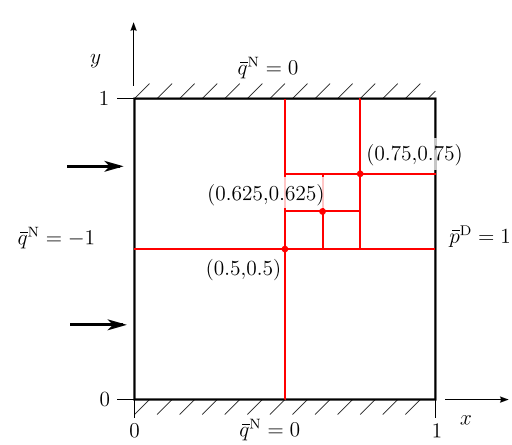


**Fig. 8.** Benchmark 1: Domain and boundary conditions.

**Table 2**
Grids for Benchmark 1.

| Method | d.o.f. | ♯-matr | ♯-frac |
|---|---|---|---|
| Box | 577 | 1078 triangles | 74 |
| TPFA | 1481 | 1386 triangles | 95 |
| MPFA | 1439 | 1348 triangles | 91 |
| EDFM | 1501 | 1369 quads | 132 |
| Flux-Mortar | 3366 | 1280 triangles | 75 |
| P-XFEM | 1650 | 961 quads | 164 |
| D-XFEM | 4474 | 1250 triangles | 126 |
| MFD | 2,352,280 | 1,136,456 quads | 38,600 |

elements in its normal direction and becomes coarser away from the fractures. It has a total of 1,175,056 elements.

The first distinction between the different schemes are given in Table 2, where the number of degrees of freedom, matrix elements (♯-matr) and fracture elements (♯-frac) for all the participating methods are listed. The corresponding grids are visualized in Fig. 9.

#### 4.1.1. Conductive fracture network

First, we consider a highly conductive network by setting $k_{f,n} = k_{f,t} = 10^4$. The pressure distribution of the corresponding reference solution is shown in Fig. 10. The pressure distributions given by the different methods are first compared along two lines, one horizontal at $y = 0.7$ and one vertical at $x = 0.5$. As shown in Fig. 11, all results are relatively close to the reference solution. Qualitatively, we observe that P-XFEM produces a more diffuse pressure profile in the vertical fracture.

Table 3 lists the errors with respect to the equi-dimensional reference solution for the different methods; particularly, the error for the matrix domain and the one along the two fractures. Moreover, it provides the density of the associated matrix and its condition number for each method. The performance of the methods is comparable as shown by both the matrix and the fracture errors. In fact, since the degree of sparsity does not differ significantly either, the only notable differences between the methods are the number of degrees of freedom and the condition numbers, as shown in the last column of Table 3. In that context, the Flux-Mortar and D-XFEM are clear outliers, containing a large number of degrees of freedom due to the incorporated flux variable and resulting in high condition numbers. Nevertheless, the P-XFEM scheme exhibits the highest condition number, although it has significantly fewer degrees of freedom than Flux-Mortar and D-XFEM.

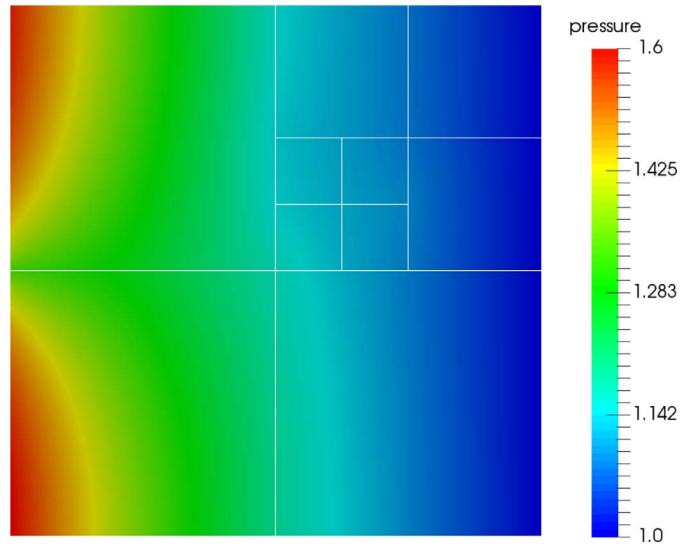


**Fig. 10.** Benchmark 1 with conductive fractures: pressure reference solution.

In addition to evaluating each method on a single grid, we perform a convergence study by choosing the grids above as initial ones and refining them twice. The results are shown in Fig. 12, detailed numbers are provided in Appendix A. For each method, the matrix error $err_m$ and fracture error $err_f$ is plotted against the square root of the number of matrix cells and against the number of fracture cells, respectively. As suggested by the numbers for the initial grids from Table 3, all methods exhibit a similar behaviour. For the matrix error in particular, the methods are very close to each other and all of them show a linear error decay. Concerning the fracture error, the XFEM methods perform a bit worse than the other ones in terms of absolute numbers. An obvious positive outlier is the fracture error for Box, which stagnates at a level much lower than all other methods. An explanation for this behaviour is still lacking. All other methods exhibit a linear error decay also for the fracture error.

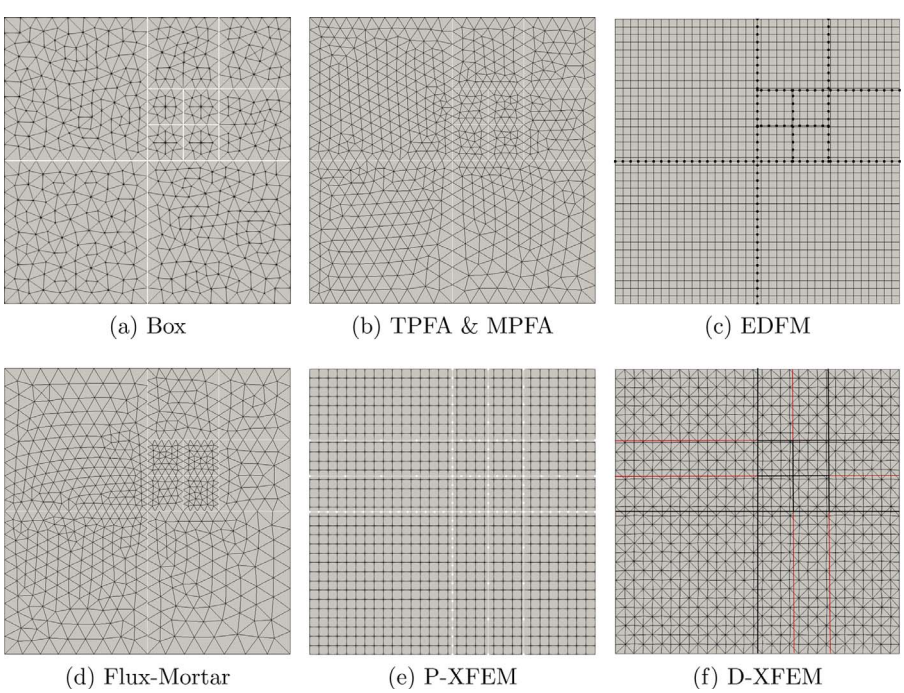


**Fig. 9.** Benchmark 1: the grids used by the different methods. In the D-XFEM grid the red lines indicate the virtual extension of the fractures up to the boundary. The fracture network has also been virtually extended for the application of P-XFEM. (For interpretation of the references to colour in this figure legend, the reader is referred to the web version of this article.)

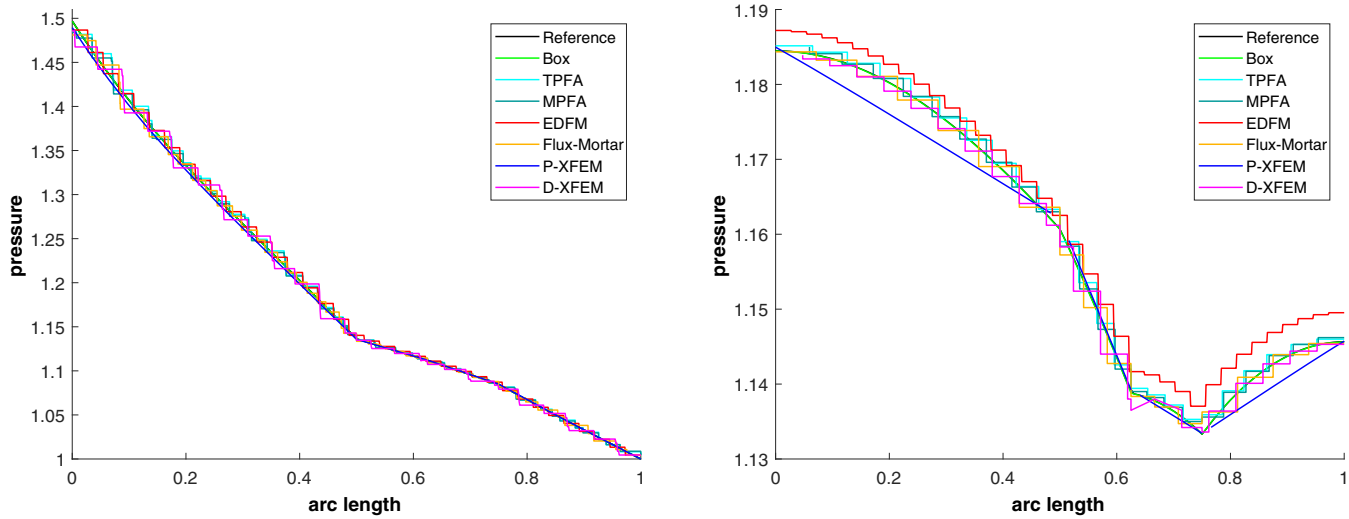


(a) Horizontal line at $y = 0.7$. (b) Longest vertical fracture at $x = 0.5$.

**Fig. 11.** Benchmark 1 with conductive fractures: comparison of values along two lines. The reference solution is hidden by the Box solution.

**Table 3**
Errors and matrix characteristics for Benchmark 1 with conductive fractures.

| Method | $err_{\mathrm{m}}$ | $err_{\mathrm{f}}$ | nnz/size$^2$ | $\|\cdot\|_2$-cond |
|---|---|---|---|---|
| Box | 1.1e−2 | 1.9e−4 | 1.1e−2 | 2.2e3 |
| TPFA | 1.1e−2 | 4.4e−3 | 2.7e−3 | 4.8e4 |
| MPFA | 1.1e−2 | 4.5e−3 | 8.0e−3 | 5.8e4 |
| EDFM | 6.5e−3 | 4.0e−3 | 3.3e−3 | 5.6e4 |
| Flux-Mortar | 1.0e−2 | 6.9e−3 | 1.8e−3 | 2.4e6 |
| P-XFEM | 9.3e−3 | 7.3e−3 | 8.0e−3 | 9.3e9 |
| D-XFEM | 9.6e−3 | 8.9e−3 | 1.3e−3 | 1.2e6 |

### 4.1.2. Blocking fracture network

We now assume a blocking fracture network by setting $k_{\mathrm{f,n}} = k_{\mathrm{f,t}} = 10^{-4}$. The pressure distribution of the corresponding reference solution is shown in Fig. 13. The results clearly show the pressure discontinuities reminiscent of the low fracture permeability.

Fig. 14 compares the results of the different methods along a diagonal line crossing the whole domain from (0.0, 0.1) to (0.9, 1.0). The errors, sparsity densities, and condition numbers for the different methods are given in Table 4.

In the case of blocking fractures, the distinction between the

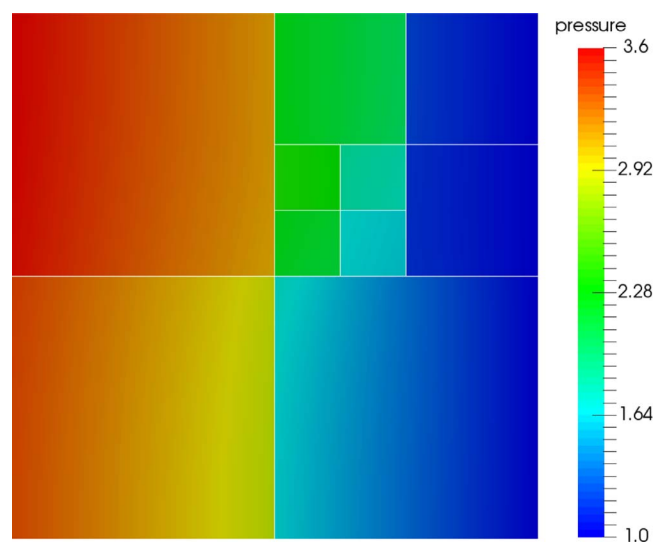


**Fig. 13.** Benchmark 1 with blocking fractures: pressure reference solution.

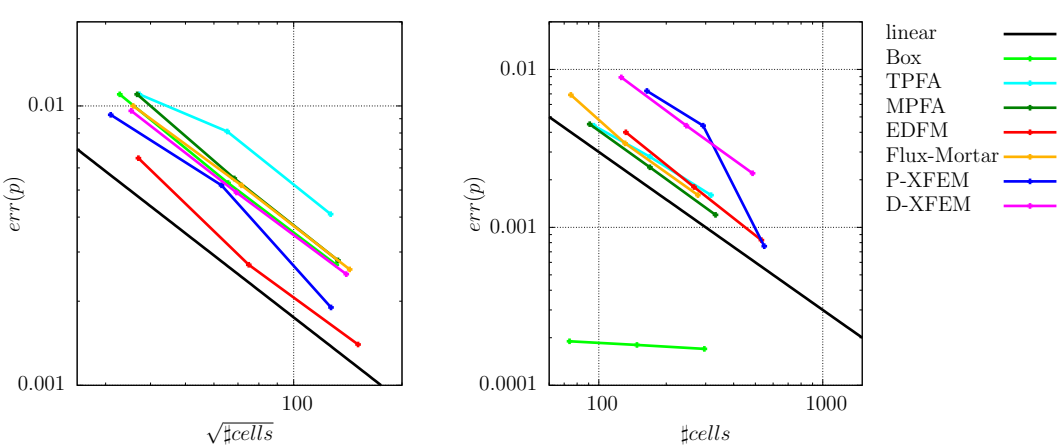


(a) Matrix error $err_{\mathrm{m}}$. (b) Fracture error $err_{\mathrm{f}}$.

**Fig. 12.** Benchmark 1 with conductive fractures: evolution of the matrix and fracture errors over grid refinement.

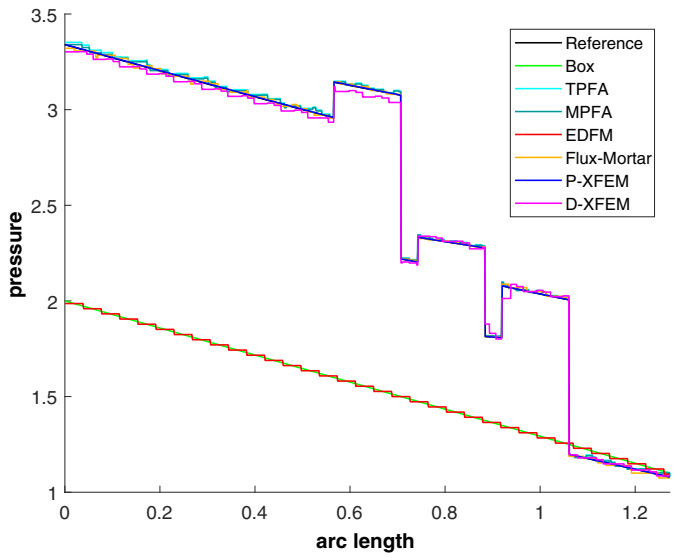


**Fig. 14.** Benchmark 1 with blocking fractures: values along the line (0.0, 0.1) − (0.9, 1.0). The reference solution is hidden by the P-XFEM solution.

**Table 4**
Errors and matrix characteristics for Benchmark 1 with blocking fractures.

| Method | $err_{\mathrm{m}}$ | $err_{\mathrm{f}}$ | nnz/size$^2$ | $\|\cdot\|_2$-**cond** |
|---|---|---|---|---|
| Box | 4.1e−1 | 3.2e−1 | 1.1e−2 | 1.3e3 |
| TPFA | 5.6e−3 | 4.4e−3 | 2.7e−3 | 2.6e4 |
| MPFA | 4.4e−3 | 3.6e−3 | 2.7e−3 | 6.3e4 |
| EDFM | 2.9e−1 | 3.2e−1 | 3.3e−3 | 9.2e3 |
| Flux-Mortar | 4.3e−3 | 4.6e−3 | 1.6e−3 | 9.0e2 |
| P-XFEM | 2.7e−3 | 2.0e−2 | 6.9e−3 | 1.3e7 |
| D-XFEM | 1.0e−2 | 1.8e−2 | 1.3e−3 | 2.2e6 |

different methods is more apparent. As mentioned above, the Box and EDFM schemes are unable to capture the resulting pressure discontinuities. As a result, these methods show large errors in both the matrix and the fracture domains. The remaining methods, which are capable of handling discontinuities, differ a bit more among each other in terms of fracture and matrix errors. The condition numbers have improved significantly for the Flux-Mortar and P-XFEM schemes. Conversely, for TPFA, MPFA and D-XFEM, condition numbers for the blocking fractures case are similar to those obtained for the permeable fractures case.

We investigate the error decays also for the variant of blocking fractures. The decays are illustrated in Fig. 15. The spread between the different methods becomes very explicit here. As to be expected, the errors for Box and EDFM do not improve with grid refinement. Concerning the matrix error, TPFA, MPFA, Flux-Mortar and P-XFEM exhibit a linear decay, while D-XFEM appears to converge with an inferior order. This is due to the fact that in this method fractures are artificially extended to the boundary with a permeability that is the same of the surrounding matrix: the "T" type intersections become "X" intersections with severe permeability jumps between the two branches of the same fractures, causing numerical problems that affect convergence. Although P-XFEM shows the best numbers for the matrix error, both XFEM methods result in considerably higher fracture errors than TPFA, MPFA and Flux-Mortar. For the convergent methods, the rate of convergence for the fracture error between the second and third refinement stage is measured between 0.45 and 0.64.

### 4.2. Benchmark 2: Hydrocoin

Within the international Hydrocoin project, (Swedish Nuclear Power Inspectorate (SKI), 1987), a benchmark for heterogeneous groundwater flow problems was presented. The domain setup is shown in Fig. 16. We point out that we have slightly modified the original domain such that equi-dimensional and hybrid-dimensional models can be run on exactly the same domain. This allows for an easier comparison of the solution values over the whole domain. The exact modifications are described in Appendix B.

For this case, we keep the original formulation in terms of the piezometric head and the hydraulic conductivity instead of pressure and permeability. In particular, the boundary conditions are Dirichlet piezometric head on the top boundary and Neumann no flow on the other three boundaries. The permeability is $10^{-6}$ m/s in the fracture zones and $10^{-8}$ m/s in the rock matrix respectively.

Table 5 lists the number of degrees of freedom, matrix elements and fracture elements for all the participating methods.

The corresponding grids are visualized in Fig. 17.

The original benchmark shows the piezometric head distribution along five horizontal lines through the modeled domain. Here, we first show in Fig. 18 the plot at a depth of 200 m, as indicated by the dashed line in Fig. 16. All participating methods show a good agreement with the reference solution. Only the EDFM method is a bit off. We remark that the plots for the methods employing cell-wise constant solution values exhibit staircase-like patterns corresponding to these values.

Table 6 lists the errors for the different methods. The uniform behaviour exhibited in Fig. 18 is reflected by the error values. Especially the errors in the matrix domain are within very narrow bounds, while the fracture errors show a larger variation. Just like for Benchmark 1,

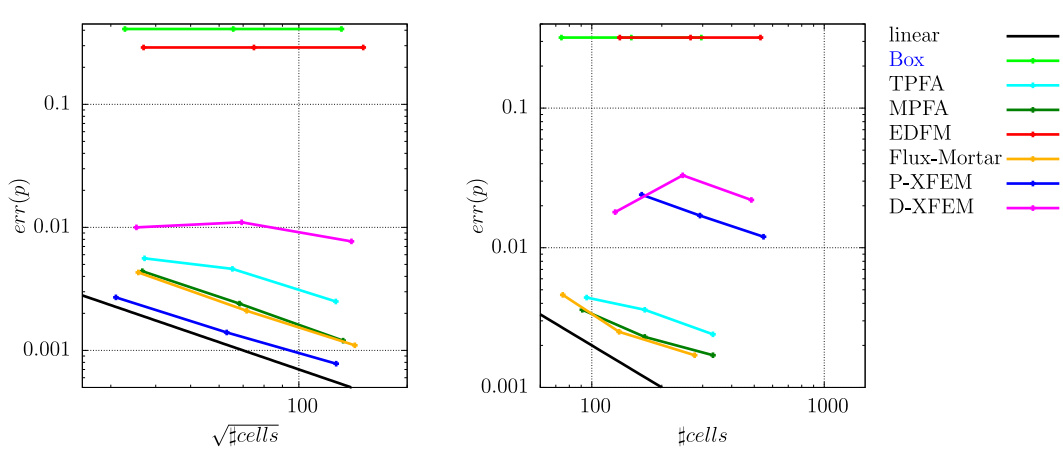


(a) Matrix error $err_{\mathrm{m}}$. (b) Fracture error $err_{\mathrm{f}}$.

**Fig. 15.** Benchmark 1 with blocking fractures: evolution of the matrix and fracture errors over grid refinement.

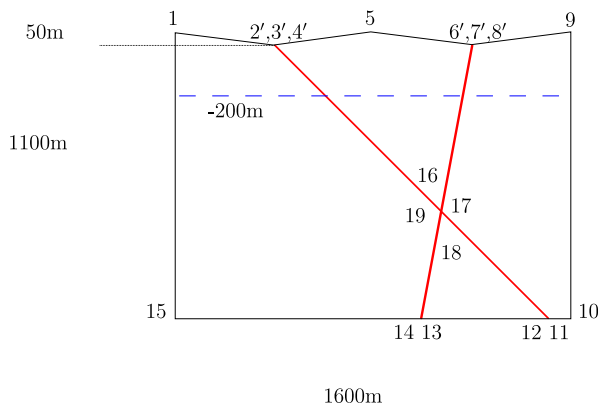


**Fig. 16.** Geometry of the modeled domain of the Hydrocoin test case 2, Swedish Nuclear Power Inspectorate (SKI) (1987). Modified node locations are indicated by numbers superscripted with ′. Boundary conditions are hydraulic head on top and Neumann no-flow on the other three sides of the domain.

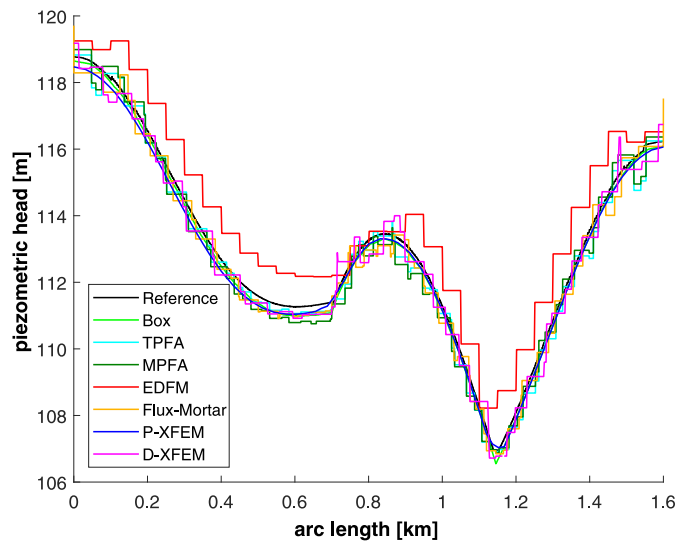


**Fig. 18.** Benchmark 2: head values along a horizontal line at a depth of 200 m.

**Table 5**
Grids for Benchmark 2.

| Method | d.o.f. | #-matr | #-frac |
|---|---|---|---|
| Box | 1496 | 2863 triangles | 74 |
| TPFA | 1459 | 1416 triangles | 43 |
| MPFA | 1532 | 1416 triangles | 43 |
| EDFM | 1044 | 960 quads | 84 |
| Flux-Mortar | 3647 | 1384 triangles | 63 |
| P-XFEM | 1667 | 1320 quads | 68 |
| D-XFEM | 3514 | 1132 triangles | 160 |
| MFD | 889,233 | 424,921 mixed | 19,287 |

**Table 6**
Errors and matrix characteristics for Benchmark 2.

| method | $err_m$ | $err_f$ | nnz/size$^2$ | $\|\cdot\|_2$-cond |
|---|---|---|---|---|
| Box | 9.2e−3 | 3.3e−3 | 4.5e−3 | 5.4e3 |
| TPFA | 1.1e−2 | 1.1e−2 | 2.7e−3 | 3.5e4 |
| MPFA | 9.3e−3 | 6.8e−3 | 8.2e−3 | 6.6e4 |
| EDFM | 1.5e−2 | 8.3e−3 | 4.7e−3 | 3.9e4 |
| Flux-Mortar | 1.0e−2 | 7.2e−3 | 1.5e−3 | 9.0e12 |
| P-XFEM | 1.2e−2 | 3.2e−3 | 6.5e−3 | 2.7e9 |
| D-XFEM | 1.2e−2 | 6.9e−3 | 1.7e−3 | 6.2e12 |

remarkably high differences can be observed for the matrix condition numbers. While the ones for Box, TPFA, MPFA and EDFM are on the order of $10^4$, the one for P-XFEM is five orders and the ones for Flux-Mortar and D-XFEM are even seven orders of magnitude larger, due to their saddle-point nature.

We remark that the fracture apertures are, with around 10m, rather high in relation to the dimensions of the computational domain ( ~ 1000 m) and the element sizes ( ~ 50 m) employed in the calculations above. Therefore, the assumption of a negligible aperture that justifies the usage of hybrid-dimensional methods is questionable. This is confirmed by the fact that no convergence can be observed for the considered methods when refining the grids depicted in Fig. 17. The total error is already dominated by the modeling error rather than the discretization error. Since our focus is on comparing different DFM methods that all rely on this assumption, we refrain from performing a more detailed analysis in this direction.

We would like to point out that an aperture of 10 m and more is often encountered in real field problems. The original intention of the Hydrocoin groups was to have a representation of a highly conductive fault zone: “The problem is an idealisation of the hydrogeological conditions encountered at a potential site for a deep repository in bedrock” (Swedish Nuclear Power Inspectorate (SKI), 1987). Some examples on modeling the impact of hydraulic fracturing on groundwater where the fault widths range between 10 and 30 m are provided in

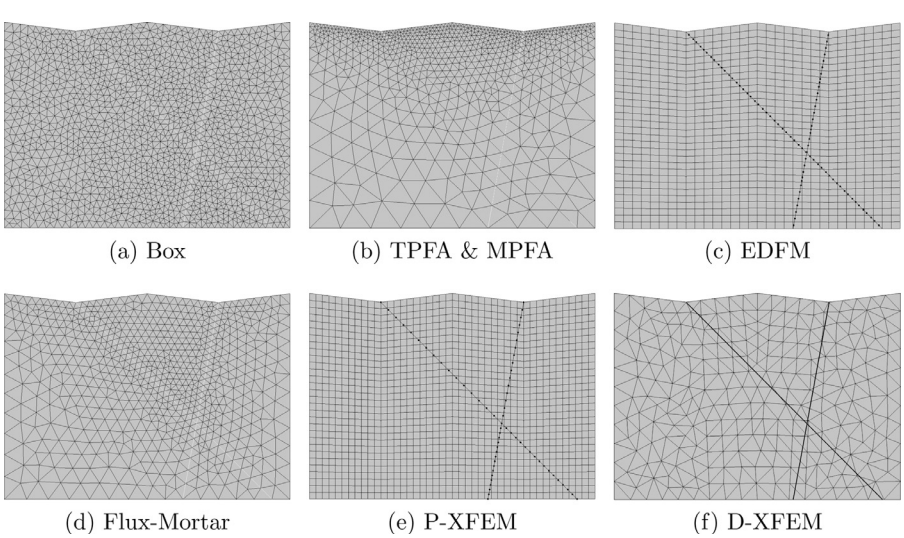


**Fig. 17.** Benchmark 2: the grids used by the different methods.

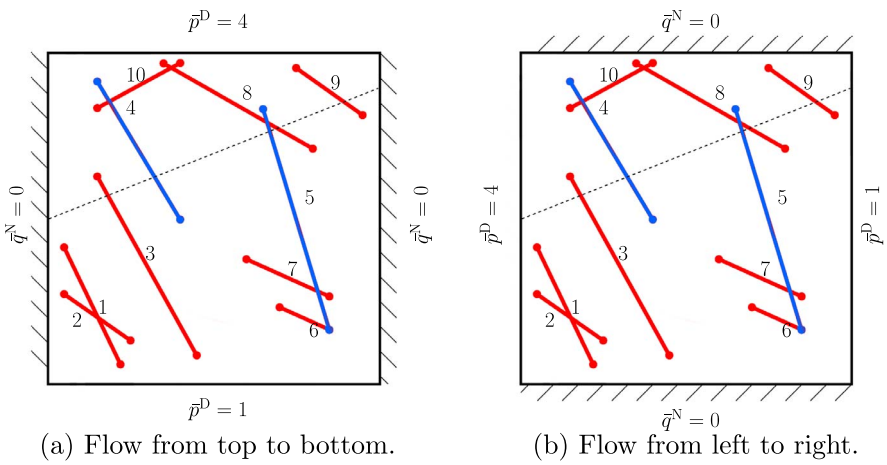


(a) Flow from top to bottom. (b) Flow from left to right.

**Fig. 19.** Benchmark 3: Domain and boundary conditions for cases (a) and (b). The red fractures are conductive, the blue ones are blocking. The dashed line is chosen to compare pressure profiles across both blocking and permeable fractures. (For interpretation of the references to colour in this figure legend, the reader is referred to the web version of this article.)

Gassiat et al. (2013), Pfunt et al. (2016) and Taherdangkoo et al. (2017). It is common practice and, depending on the geometrical complexity, often the only efficient possibility to treat such fault zones with lower-dimensional models. A modeler parametrizing a real field problem will often face the question of how to consider the fractures in the model. Despite the fact that the assumption of a negligible aperture is not justified, the accuracy of a hybrid-dimensional approach might still be acceptable, as is also indicated by our results.

### 4.3. Benchmark 3: complex fracture network

This test case considers a small but complex fracture network that includes permeable and blocking fractures. The domain and boundary conditions are shown in Fig. 19. The exact coordinates for the fracture positions are provided in Appendix C. The fracture network contains ten straight immersed fractures, grouped in disconnected networks. The aperture is $\varepsilon = 10^{-4}$ for all fractures, and the permeability is $k_{f,n} = k_{f,t} = 10^4$ for all fractures except for fractures 4 and 5, which are blocking fractures with $k_{f,n} = k_{f,t} = 10^{-4}$. The matrix permeability is again set to $\mathbb{K}_m = \mathbb{I}$. Note that we are considering two sub-cases, a) and b). with a pressure gradient which is predominantly vertical and horizontal, respectively, to better highlight the impact of the blocking fractures. The corresponding reference solutions are depicted in Fig. 20.

Table 7 lists the number of degrees of freedom, matrix elements and fracture elements for all the participating methods. The corresponding grids are visualized in Fig. 21.

The P-XFEM method could not participate in this benchmark example. Its current implementation requires that each matrix element face is cut by at most one fracture branch. While it would be possible to construct a matrix grid that satisfies this requirement, this would contradict the promised advantage of admitting independent fracture and matrix grids.

**Table 7**
Grids for Benchmark 3.

| Method | d.o.f. | #-matr | #-frac |
|---|---|---|---|
| Box | 1373 | 2664 triangles | 152 |
| TPFA | 1420 | 1332 triangles | 88 |
| TPFA* | 1425 | 1332 triangles | 93 |
| MPFA | 1500 | 1332 triangles | 88 |
| EDFM | 1572 | 1369 quads | 203 |
| Flux-Mortar | 3349 | 1230 triangles | 89 |
| D-XFEM | 7180 | 1922 triangles | 199 |
| MFD | 3,471,040 | 2,260,352 triangles | 52,608 |

#### 4.3.1. Flow from top to bottom

We first consider the setup depicted in Fig. 19(a), resulting in the reference solution visualized in Fig. 20(a). Table 8 lists the errors for this first variant, namely, the flow from top to bottom.

The pressure profiles along the line (0, 0.5) − (1, 0.9), computed by the different methods, are represented in Fig. 22: one can observe that most methods are in good agreement with the reference solution, except for EDFM and the Box method that cannot represent the behaviour of the blocking fractures. Even though this is still a synthetic case, we can see that the geometry of the network starts to be an issue: relatively small intersection angles are present, for instance, between fractures 1 and 2. Another difficulty consists in the coexistence of permeable and blocking fractures which intersect each other: on one hand, some of the methods are not well suited to describe a blocking behaviour, on the other hand, the coupling conditions at the intersection become less trivial in these cases. All the participating methods that account explicitly for the effect of permeability at the fracture intersections have adopted the harmonic average in the case of a permeable and a

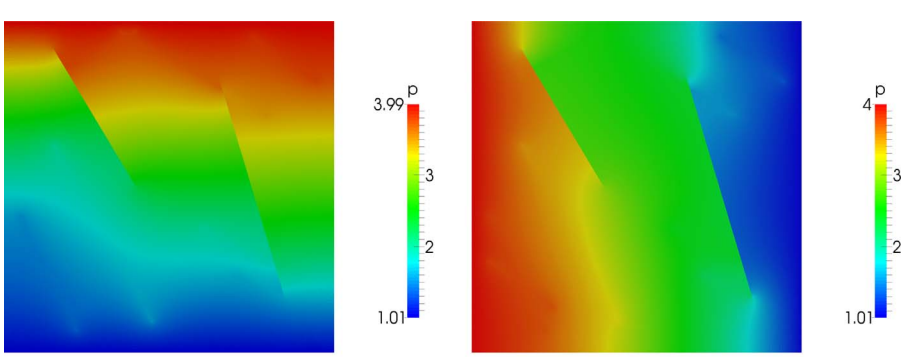


(a) Flow from top to bottom. (b) Flow from left to right.

**Fig. 20.** Benchmark 3: reference solution for cases a) and b).

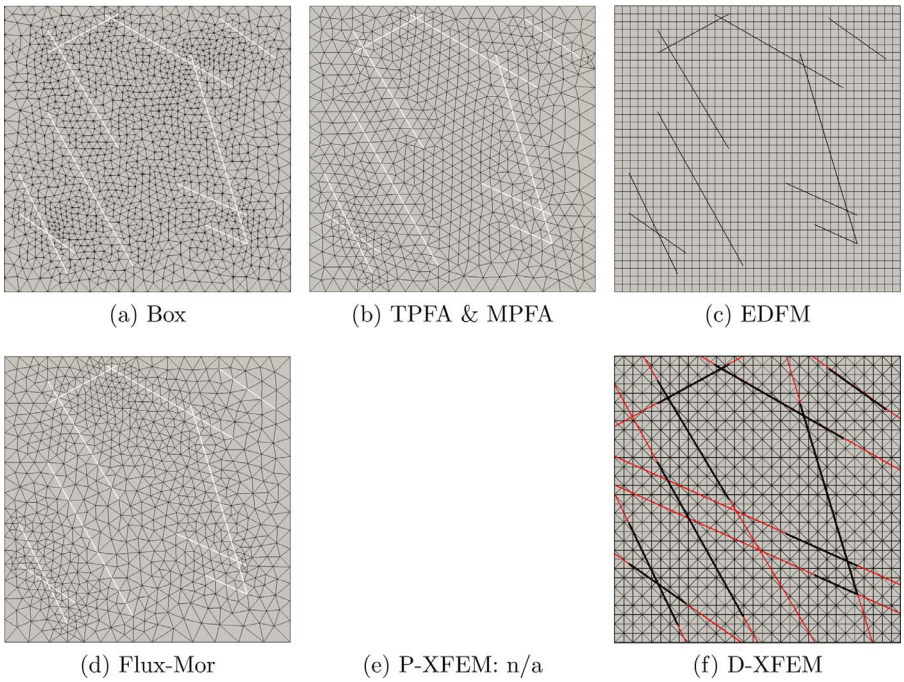


**Fig. 21.** Benchmark 3: the grids used by the different methods. In the DXFEM grid the red lines indicate the virtual extension of the fractures up to the boundary. (For interpretation of the references to colour in this figure legend, the reader is referred to the web version of this article.)

**Table 8**
Errors and matrix characteristics for the first variant of Benchmark 3.

| Method | $err_m$ | $err_f$ | nnz/size$^2$ | $\|\cdot\|_2$-cond |
|---|---|---|---|---|
| Box | 4.9e−2 | 3.4e−2 | 4.9e−3 | 4.3e3 |
| TPFA | 2.7e−2 | 2.9e−2 | 2.8e−3 | 2.6e4 |
| TPFA* | 1.3e−2 | 1.1e−2 | 2.8e−3 | 7.9e4 |
| MPFA | 2.5e−2 | 2.8e−2 | 8.5e−3 | 2.5e4 |
| EDFM | 3.8e−2 | 4.5e−2 | 3.1e−3 | 1.2e6 |
| Flux-Mortar | 1.0e−2 | 8.2e−3 | 1.6e−3 | 1.3e4 |
| D-XFEM | 1.9e−2 | 2.9e−2 | 8.2e−4 | 8.1e3 |

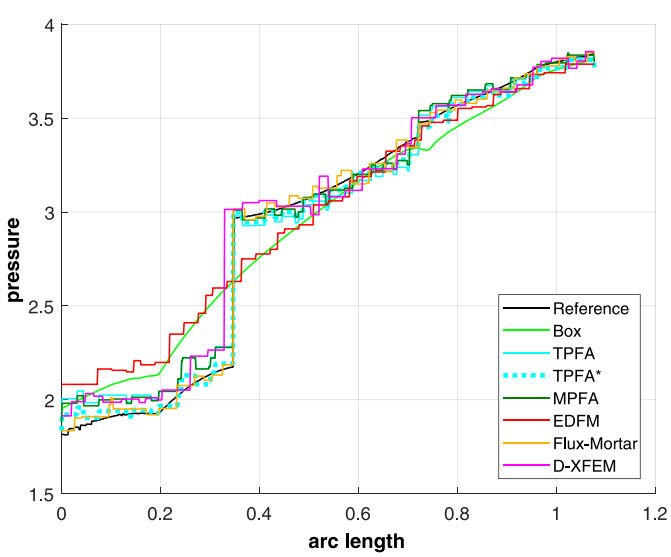


**Fig. 22.** Benchmark 3, first variant: pressure values along the line (0.0, 0.5) − (1.0, 0.9).

blocking fracture crossing each other. The errors reported in Table 8 show that the methods requiring the continuity of pressure (EDFM and the Box) exhibit slightly higher errors in the matrix. However, the difference is not particularly sharp, since in this sub-case the average pressure gradient is almost parallel to the blocking fractures. The elimination of the fracture intersection cells in the TPFA and MPFA methods is ill-suited for cases where fractures of different permeability cross. Therefore, we include a solution TPFA* in which we have not performed the removal. The corresponding results show a far smaller error compared to the TPFA with elimination, but also demonstrate that the elimination significantly increases the condition number.

Like for Benchmark 1, we investigate the errors in the matrix and in the fracture network, see Fig. 23 and detailed numbers in Appendix D. We have not considered Box and EDFM, since the corresponding errors stagnate due to the presence of blocking fractures, as already discussed in Section 4.1.2. Surprisingly at first sight, now also TPFA and MPFA do not converge. This is an implication of the facts mentioned above, namely, that the intersection cells are removed for both methods together with the appearance of intersecting conductive and blocking fractures. When these cells are included, convergence can be achieved. Only TPFA* and Flux-Mortar exhibit a linear decay of the matrix error, while D-XFEM shows considerably higher absolute numbers and an inferior convergence rate. As already observed for the blocking variant of Benchmark 2, linear convergence cannot be achieved for the fracture error.

### 4.3.2. *Flow from left to right*

We now investigate the more challenging setup from Fig. 19(b) and its corresponding reference solution depicted in Fig. 20(b). The errors for this second variant are summarized in Table 9. The pressure profiles along the line (0, 0.5) − (1, 0.9), computed by the different methods for are represented in Fig. 24. As in the previous sub-case EDFM and the Box method are not able to capture the pressure jumps across the blocking fractures. Moreover, the D-XFEM method underestimates the second pressure jump. This behaviour will also reflect in a poor convergence rate (see Fig. 25). In this second case, since we impose pressure on the sides of the square domain, the solution is more challenging. As we can observe from Fig. 20, the gap between continuous and discontinuous methods increases.The errors remain of the same order of magnitude, indicating that all the methods capture the overall trend of the solution. Nevertheless, the difference between TPFA/MPFA and TPFA* becomes larger, indicating that it is even more important to treat

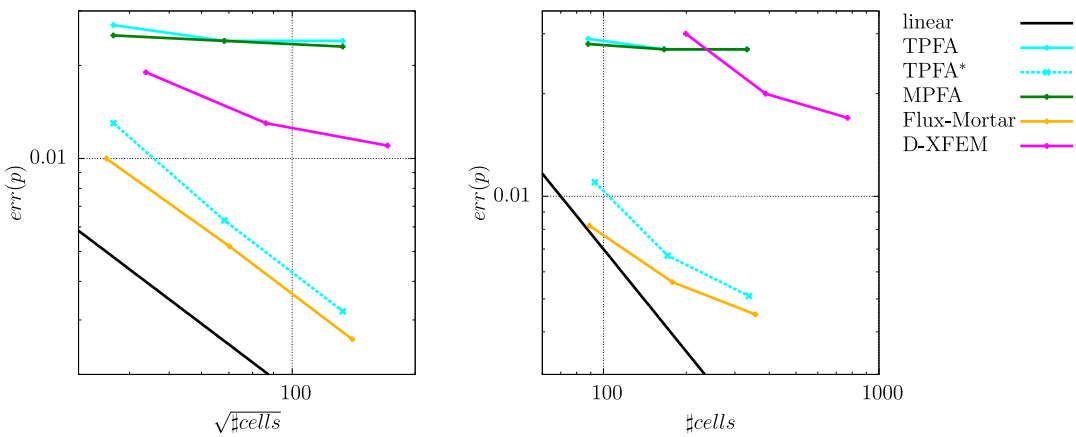


(a) Matrix error $err_{\mathrm{m}}$. (b) Fracture error $err_{\mathrm{f}}$.

**Fig. 23.** Benchmark 3, flow from top to bottom: evolution of the matrix and fracture errors over grid refinement.

**Table 9**
Errors and matrix characteristics for the second variant of Benchmark 3.

| method | $err_{\mathrm{m}}$ | $err_{\mathrm{f}}$ | nnz/size$^2$ | $\|\cdot\|_2$-cond |
|---|---|---|---|---|
| Box | 7.5e−2 | 6.3e−2 | 4.9e−3 | 5.3e3 |
| TPFA | 5.1e−2 | 6.7e−2 | 2.8e−3 | 3.1e4 |
| TPFA* | 1.3e−2 | 1.1e−2 | 2.8e−3 | 2.0e5 |
| MPFA | 5.1e−2 | 6.7e−2 | 8.5e−3 | 3.1e4 |
| EDFM | 5.8e−2 | 8.9e−2 | 3.1e−3 | 1.2e6 |
| Flux-Mortar | 1.4e−2 | 1.3e−2 | 1.6e−3 | 1.4e4 |
| D-XFEM | 2.2e−2 | 3.6e−2 | 8.2e−4 | 8.1e3 |

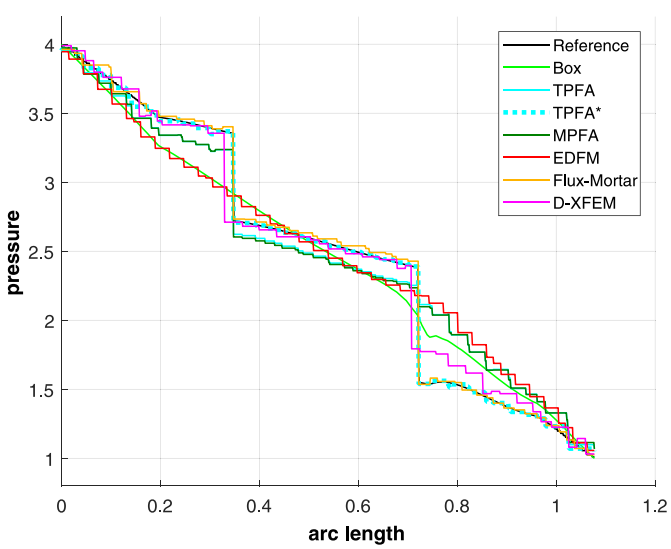


**Fig. 24.** Benchmark 3, second variant: pressure values along the line (0.0, 0.5) − (1.0, 0.9).

properly the intersections of conductive and blocking fractures.

The error plots associated with this second variant are shown in Fig. 25. They are very similar to the first variant, the only remarkable difference being the stagnation in the numbers for D-XFEM. This is once again caused by the intersections between fractures with different permeabilities, particularly in the "virtual" extensions of the fractures to the boundary.

### 4.4. Benchmark 4: a realistic case

In this last test case we consider a real set of fractures from an interpreted outcrop in the Sotra island, near Bergen in Norway. The set is composed of 64 fractures grouped in 13 different connected networks, ranging from isolated fractures up to tens of fractures each. In the interpretation process two fractures were composed by more than one segment. However, since the implementation of some methods relay on the fact that one fracture is represented by a single geometrical object, we substitute them by a single segment. It is worth to notice that we are changing the connectivity of the system, nevertheless our goal is to make a comparison of the previous schemes on a complex and realistic set of fractures. The interpreted outcrop and the corresponding set of fractures are represented in Fig. 26. The size of the domain is 700 m × 600 m with uniform matrix permeability $\mathbb{K}_{\mathrm{m}} = 10^{-14}\mathbb{I}\,\mathrm{m}^2$. For simplicity all the fractures have the same scalar permeability $k_{\mathrm{f,n}} = k_{\mathrm{f,t}} = 10^{-8}\,\mathrm{m}^2$, and aperture $10^{-2}$ m. We consider no-flow boundary condition on top and bottom, pressure 1013250 Pa on the left, and pressure 0 Pa on the right of the boundary of the domain. Due to the high geometrical complexity of the fracture network not all involved numerical schemes/simulators could be used. Nevertheless, it is worth to point out that for the others the main difficulty in handling such geometry is an implementation issue rather than a limitation of the scheme. It is also a very tedious task to create a full-dimensional description of the fracture network and a corresponding equi-dimensional grid of the whole computational domain. Therefore, we refrain from calculating a reference solution with the MFD method and perform a direct comparison of the hybrid-dimensional methods. Since all fractures are conductive and their aperture is negligibly small, we consider all participating methods to be verified by means of the benchmark cases above.

Table 10 lists the number of degrees of freedom, the density of the associated matrix, and its condition number for the different methods. Due to the geometrical difficulties of the network the request of having a similar number of degrees of freedom among the methods is relaxed, as Table 10 indicates. Considering Fig. 27, the solutions are reported for the four methods. We notice that, except for the top right part of the domain in the Box method, the solutions are similar and comparable, which is an indication of their correctness. Compared to the previous test cases the mesh generation is the main concern and some of the methods require a fine tuning to avoid non-physical connections among

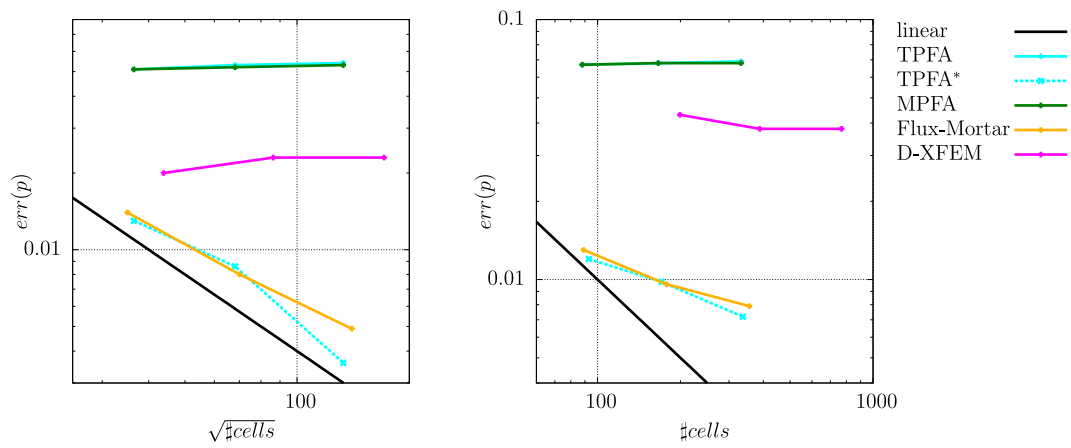


(a) Matrix error $err_{\mathrm{m}}$. (b) Fracture error $err_{\mathrm{f}}$.

**Fig. 25.** Benchmark 3, flow from left to right: evolution of the matrix and fracture errors over grid refinement.

elements where the fracture are close. An example can be found in the middle of the domain and reported in Fig. 28. Only EDFM is more robust with respect to this constraint. To present a more detailed comparison among the methods, Fig. 29 represents the pressure solution along two different lines: for $y = 500$ m and for $x = 625$ m. We note that the methods behave similarly, and the Box slightly overestimates some peaks. The oscillation of the methods are related to mesh effects.

## 5. Summary and outlook

Four benchmark cases for single-phase flow in fractured porous media have been proposed and employed to compare the performances of several state-of-the-art hybrid-dimensional discrete-fracture-matrix models. If we consider the cases where all the methods are employed within the applicability range for which they were originally developed, the results are in quite good agreement. In particular, fracture networks exhibiting a larger permeability than the surrounding matrix can be accurately described by all methods. On the other hand, not all methods are capable of modeling blocking fractures. In this case, some methods fail to predict the correct flow patterns for the corresponding scenarios. These observations are confirmed by investigating the behaviour of the errors with respect to the equi-dimensional reference solution under mesh refinement. For purely conductive fracture networks, all methods exhibit a linear decay for both the error in the matrix and the fractures, and the total numbers are very similar. The fact that some methods cannot deal with blocking fractures is reflected by a stagnation of the corresponding errors. In the presence of blocking fractures, the order of convergence for the fracture error decreases for all methods. Moreover, the fracture error for the XFEM methods has been observed to be considerably larger than for the other convergent methods. Even if a method can handle conductive and blocking fractures, the intersection of a conductive with a blocking fracture branch poses additional challenges. In this case, a method may not converge if it doesn't treat these intersections carefully enough. Of the eight participating methods, only two, TPFA* and Flux-Mortar, proved to be convergent through all considered cases.

Apart from the discretization error, another component of the total error is the modeling error resulting from the assumption that the fracture apertures are negligibly small. For the Hydrocoin benchmark, this component obviously dominated the measured error. More detailed

**Table 10**
Discretization and matrix characteristics for Benchmark 4.

| Method | d.o.f. | ♯-matr | ♯-frac | nnz/size$^2$ | $\|\cdot\|_2$-cond |
|---|---|---|---|---|---|
| Box | 5563 | 10,807 triangles | 1386 | 1.2e−3 | 9.3e5 |
| TPFA | 8481 | 7614 triangles | 867 | 4.9e−4 | 5.3e6 |
| MPFA | 8588 | 7614 triangles | 867 | 1.6e−3 | 4.9e6 |
| EDFM | 3599 | 2491 quads | 1108 | 1.4e−3 | 4.7e6 |
| Flux-Mortar | 25,258 | 8319 triangles | 1317 | 2.0e−4 | 2.2e17 |

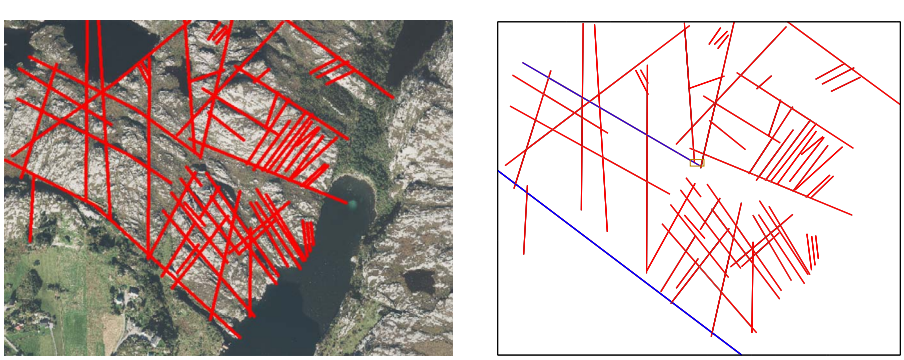

**Fig. 26.** In the left the interpretation of the set of fractures superimposed to the map. In the right the geometry used in the simulations. The rectified fractures are depicted in blue. (For interpretation of the references to colour in this figure legend, the reader is referred to the web version of this article.)

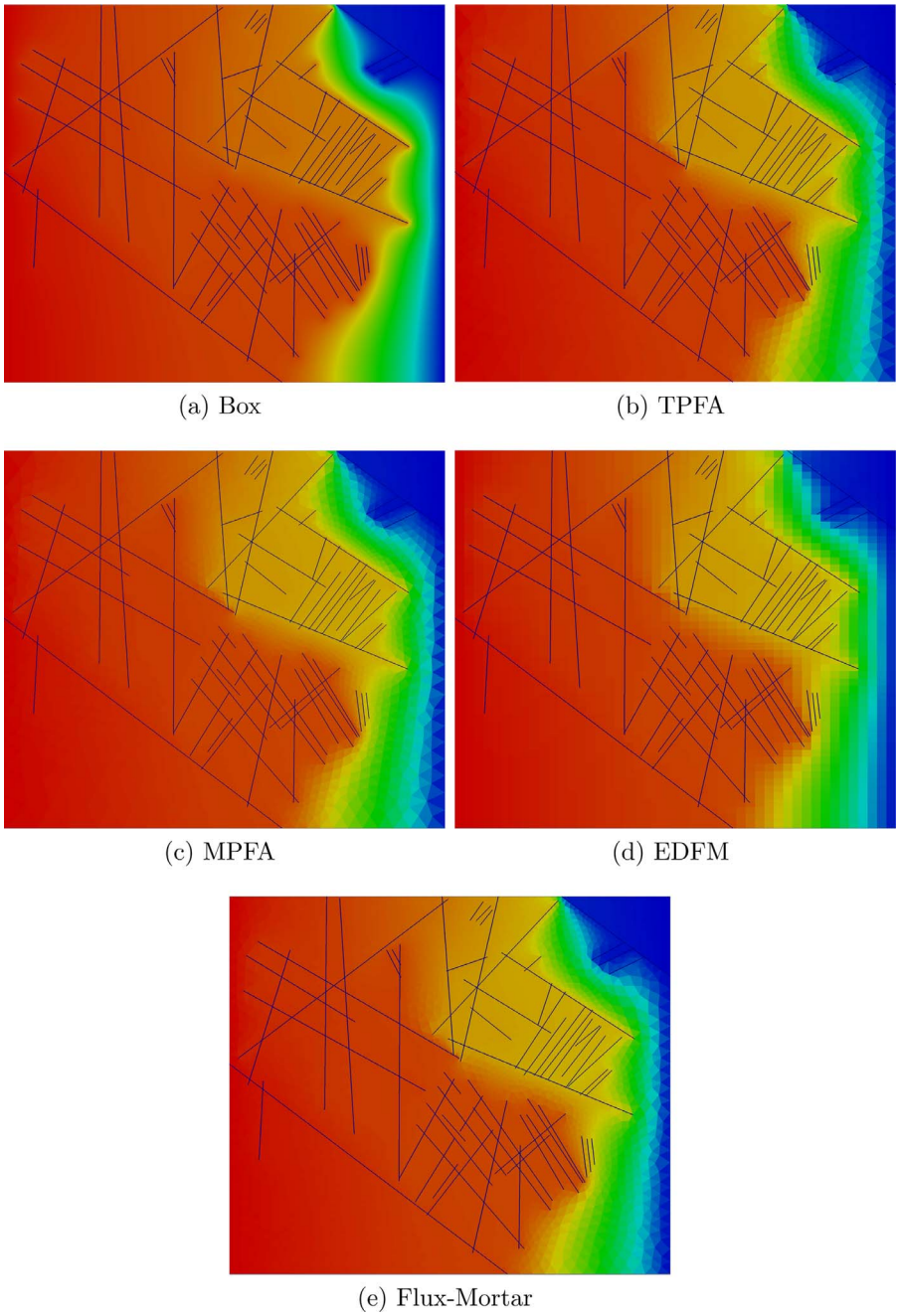


**Fig. 27.** Representation of the matrix pressures field for the realistic case. The solution values range between 0 and 1013250 Pa.

investigations on the relation between these two components is an interesting topic for future work.

Especially noteworthy are the large differences in the condition numbers of the associated system matrices. The effect of these differences on the behaviour of linear solvers is difficult to quantify in a comparable manner, since the different methods pose different requirements for such solvers.

In principle, all participating methods should have been able to run all proposed cases. However, due to implementation restrictions, some methods could not perform the cases with more complex fracture network geometries. Even if the methodology is general enough, technical difficulties can become crucial obstacles to tackling realistic scenarios.

All the investigated benchmarks are restricted to simple physics and two-dimensional computational domains. This should give other researchers developing DFM models the chance to perform comparison studies for their methods. We encourage the scientific community to contribute their results for the benchmarks to a corresponding Git repository at https://git.iws.uni-stuttgart.de/benchmarks/fracture-flow.

Further benchmark cases may be developed in the near future. In particular, we are very interested in enhancing the purely single-phase single-component flow physics by adding transport, deformation and/or reaction processes. We aim to carry out these efforts in a broader context by means of international workshops. A first such workshop “Modeling and benchmarking of fractured porous media: flow, transport and deformation” was organized by the authors and held in June 2017 at the University of Bergen. First future steps already have been discussed there.

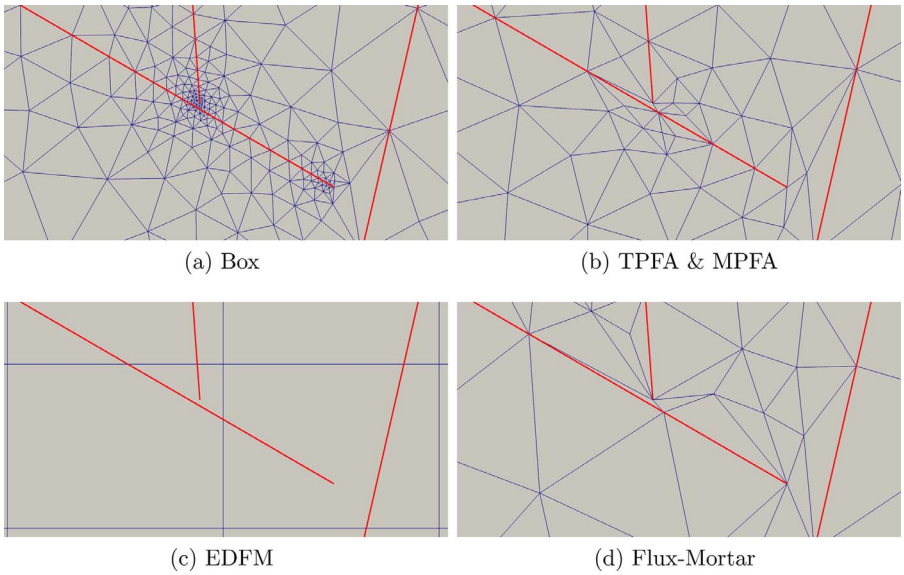


**Fig. 28.** Benchmark 4: Representation of mesh in the middle of the domain. The size of the picture is approximately 30 m × 15 m centred in (360, 350). It is represented by the small rectangle in the centre of Fig. 26 left.

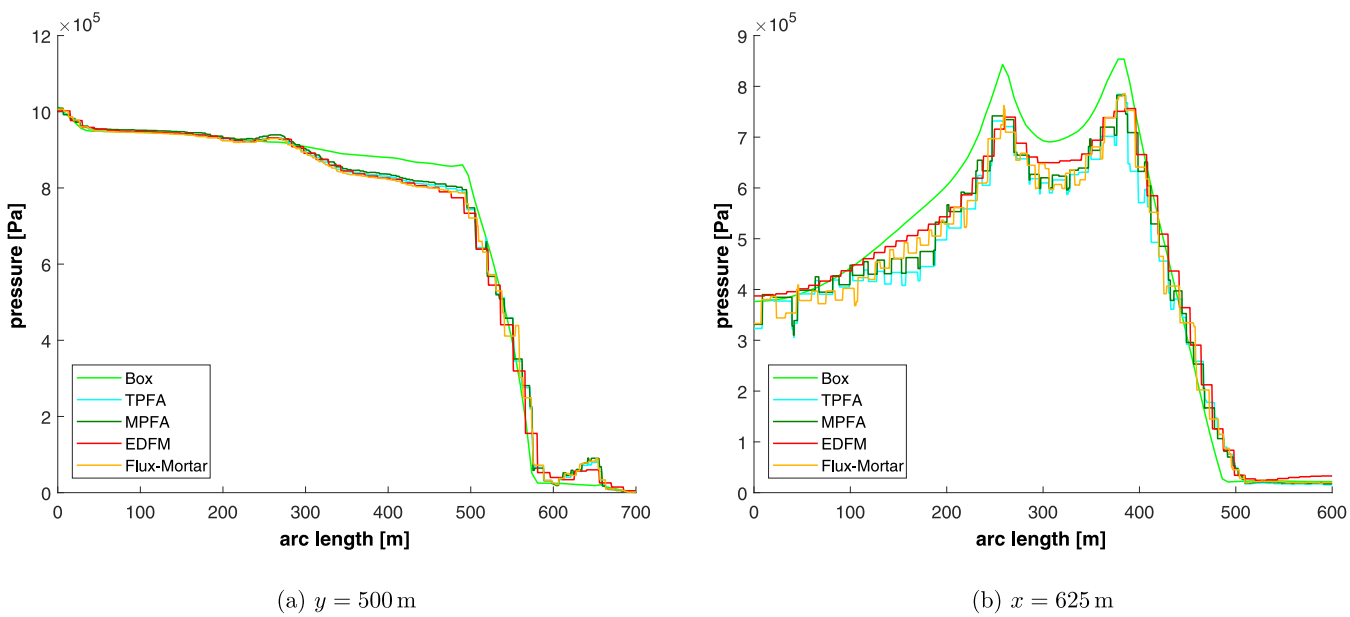


**Fig. 29.** Benchmark 4: Pressure solutions of the 4 methods plotted over lines (a) $y = 500$ m, and (b) $x = 625$ m.

## Acknowledgement

The authors warmly thank Luisa F. Zuluaga, from University of Bergen, for constructing and providing the real fracture network for the example in Section 4.4. The authors wish to thank also Luca Pasquale and Stefano Zonca.

The second author acknowledges financial support from the GeoStim project from the Research Council of Norway (project no. 228832) through the ENERGIX program. The third author was supported by Norwegian Research Council grant 233736. The fourth author acknowledges financial support from the ANIGMA project from the Research Council of Norway (project no. 244129/E20) through the ENERGIX program.

## Appendix A. Details for the convergence study in Benchmark 1

Detailed numbers for the convergence studies carried out in Section 4.1 are provided by means of tables for the errors in matrix and fracture, calculated according to (7). In particular, the index $k$ in $err_{\mathrm{m},\,k}$ and $err_{\mathrm{f},\,k}$ refers to the refinement level. The number of elements is indicated correspondingly by $n_{\mathrm{m},\,k}$ and $n_{\mathrm{f},\,k}$ for matrix and fracture, respectively. The experimental orders of convergence $eoc_{\mathrm{m},\,k}$ and $eoc_{\mathrm{f},\,k}$ are calculated by

$$eoc_{\mathrm{m},k} = 2\frac{\log \dfrac{err_{\mathrm{m},k}}{err_{\mathrm{m},k-1}}}{\log \dfrac{n_{\mathrm{m},k-1}}{n_{\mathrm{m},k}}}, \quad eoc_{\mathrm{f},k} = \frac{\log \dfrac{err_{\mathrm{f},k}}{err_{\mathrm{f},k-1}}}{\log \dfrac{n_{\mathrm{f},k-1}}{n_{\mathrm{f},k}}}.$$

*A1. Conductive fracture network*

| Method | $n_{m,0}$ | $err_{m,0}$ | $n_{m,1}$ | $err_{m,1}$ | $eoc_{m,1}$ | $n_{m,2}$ | $err_{m,2}$ | $eoc_{m,2}$ |
|---|---|---|---|---|---|---|---|---|
| Box | 1078 | 1.1e−02 | 4312 | 5.3e−03 | 1.05 | 17,248 | 2.7e−03 | 0.97 |
| TPFA | 1386 | 1.1e−02 | 4269 | 8.1e−03 | 0.54 | 14,866 | 4.1e−03 | 1.09 |
| TPFA* | – | – | – | – | – | – | – | – |
| MPFA | 1348 | 1.1e−02 | 4673 | 5.5e−03 | 1.12 | 17,632 | 2.8e−03 | 1.02 |
| EDFM | 1369 | 6.5e−03 | 5625 | 2.7e−03 | 1.24 | 22,801 | 1.4e−03 | 0.94 |
| Flux-Mortar | 1280 | 1.0e−02 | 5120 | 5.2e−03 | 0.94 | 20,480 | 2.6e−03 | 1.00 |
| P-XFEM | 961 | 9.3e−03 | 3969 | 5.2e−03 | 0.82 | 16,129 | 1.9e−03 | 1.44 |
| D-XFEM | 1250 | 9.6e−03 | 4802 | 4.9e−03 | 1.00 | 19,602 | 2.5e−03 | 0.96 |

| Method | $n_{f,0}$ | $err_{f,0}$ | $n_{f,1}$ | $err_{f,1}$ | $eoc_{f,1}$ | $n_{f,2}$ | $err_{f,2}$ | $eoc_{f,2}$ |
|---|---|---|---|---|---|---|---|---|
| Box | 74 | 1.9e−04 | 148 | 1.8e−04 | 0.08 | 296 | 1.7e−04 | 0.08 |
| TPFA | 95 | 4.4e−03 | 169 | 2.8e−03 | 0.78 | 317 | 1.6e−03 | 0.89 |
| TPFA* | – | – | – | – | – | – | – | – |
| MPFA | 91 | 4.5e−03 | 169 | 2.4e−03 | 1.02 | 332 | 1.2e−03 | 1.03 |
| EDFM | 132 | 4.0e−03 | 266 | 1.8e−03 | 1.14 | 532 | 8.3e−04 | 1.12 |
| Flux-Mortar | 75 | 6.9e−03 | 131 | 3.4e−03 | 1.27 | 277 | 1.6e−03 | 1.01 |
| P-XFEM | 164 | 7.3e−03 | 292 | 4.4e−03 | 0.88 | 548 | 7.6e−04 | 2.79 |
| D-XFEM | 126 | 8.9e−03 | 246 | 4.4e−03 | 1.05 | 486 | 2.2e−03 | 1.02 |

*A2. Blocking fracture network*

| Method | $n_{m,0}$ | $err_{m,0}$ | $n_{m,1}$ | $err_{m,1}$ | $eoc_{m,1}$ | $n_{m,2}$ | $err_{m,2}$ | $eoc_{m,2}$ |
|---|---|---|---|---|---|---|---|---|
| Box | 1078 | 4.1e−01 | 4312 | 4.1e−01 | 0.00 | 17,248 | 4.1e−01 | 0.00 |
| TPFA | 1386 | 5.6e−03 | 4269 | 4.6e−03 | 0.35 | 14,866 | 2.5e−03 | 0.98 |
| TPFA* | – | – | – | – | – | – | – | – |
| MPFA | 1348 | 4.4e−03 | 4673 | 2.4e−03 | 0.98 | 17,632 | 1.2e−03 | 1.04 |
| EDFM | 1369 | 2.9e−01 | 5625 | 2.9e−01 | 0.00 | 22,801 | 2.9e−01 | 0.00 |
| Flux-Mortar | 1280 | 4.3e−03 | 5120 | 2.1e−03 | 1.03 | 20,480 | 1.1e−03 | 0.93 |
| P-XFEM | 961 | 2.7e−03 | 3969 | 1.4e−03 | 0.93 | 16,129 | 7.8e−04 | 0.83 |
| D-XFEM | 1250 | 1.0e−02 | 4802 | 1.1e−02 | −0.14 | 19,602 | 7.7e−03 | 0.51 |

| Method | $n_{f,0}$ | $err_{f,0}$ | $n_{f,1}$ | $err_{f,1}$ | $eoc_{f,1}$ | $n_{f,2}$ | $err_{f,2}$ | $eoc_{f,2}$ |
|---|---|---|---|---|---|---|---|---|
| Box | 74 | 3.2e−01 | 148 | 3.2e−01 | 0.00 | 296 | 3.2e−01 | 0.00 |
| TPFA | 95 | 4.4e−03 | 169 | 3.6e−03 | 0.35 | 317 | 2.4e−03 | 0.64 |
| TPFA* | – | – | – | – | – | – | – | – |
| MPFA | 91 | 3.6e−03 | 169 | 2.3e−03 | 0.72 | 332 | 1.7e−03 | 0.45 |
| EDFM | 132 | 3.2e−01 | 266 | 3.2e−01 | 0.00 | 532 | 3.2e−01 | 0.00 |
| Flux-Mortar | 75 | 4.6e−03 | 131 | 2.6e−03 | 1.02 | 277 | 1.7e−03 | 0.57 |
| P-XFEM | 164 | 2.4e−02 | 292 | 1.7e−02 | 0.60 | 548 | 1.2e−02 | 0.55 |
| D-XFEM | 126 | 1.8e−02 | 246 | 3.3e−02 | −0.91 | 486 | 2.2e−02 | 0.60 |

## Appendix B. Domain modifications for Benchmark 2

Table B.11 provides the exact coordinates of the points from Fig. 16.

In comparison to the original setup, the plateaus close to the upper left and right corners 1 and 9 have been omitted. Moreover, the upper ends of the two fractures have been modified according to Fig. B.30 which amounts to the changes of nodes 2–4 and 6–8.

Finally, the position of nodes 16–19 has been recalculated with higher precision. The hybrid-dimensional models do not take into account nodes 2,4,6,8 and 16–19 and combine nodes 11,12 and 13,14, since the two-dimensional fracture regions have been reduced to two intersecting straight lines.

**Table B.11**
Coordinates of the numbered points in the modeled region of the problem depicted in Fig. 16.

| pt | $x$ (m) | $z$ (m) | pt | $x$ (m) | $z$ (m) |
|---|---|---|---|---|---|
| 1 | 0 | 150 | 11 | 1505 | −1000 |
| 2′ | 394.285714286 | 100.714285714 | 12 | 1495 | −1000 |
| 3′ | 400 | 100 | 13 | 1007.5 | −1000 |
| 4′ | 404.444444444 | 100.555555556 | 14 | 992.5 | −1000 |
| 5 | 800 | 150 | 15 | 0 | −1000 |
| 6′ | 1192.66666667 | 100.916666667 | 16 | 1071.34615385 | −566.346153846 |
| 7′ | 1200 | 100 | 17 | 1084.03846154 | −579.038461538 |
| 8′ | 1207.6744186 | 100.959302326 | 18 | 1082.5 | −587.5 |
| 9 | 1600 | 150 | 19 | 1069.80769231 | −574.807692308 |
| 10 | 1600 | −1000 | | | |

**Fig. B.30.** Modifications of the Hydrocoin model domain compared to the original formulation (Swedish Nuclear Power Inspectorate (SKI), 1987). The original upper boundary is drawn with grey thin lines, while thick black lines are used for the modified boundary. Modified node locations are indicated by numbers superscripted with ′. The shaded regions show the upper parts of the two slightly extended equi-dimensional fractures.

## Appendix C. Fracture coordinates for Benchmark 3

The coordinates are listed in Table C.12.

**Table C.12**
Benchmark 3: Fracture coordinates

| Nf | xA | yA | xB | yB |
|---|---|---|---|---|
| 1 | 0.0500 | 0.4160 | 0.2200 | 0.0624 |
| 2 | 0.0500 | 0.2750 | 0.2500 | 0.1350 |
| 3 | 0.1500 | 0.6300 | 0.4500 | 0.0900 |
| 4 | 0.1500 | 0.9167 | 0.4000 | 0.5000 |
| 5 | 0.6500 | 0.8333 | 0.849723 | 0.167625 |
| 6 | 0.7000 | 0.2350 | 0.849723 | 0.167625 |
| 7 | 0.6000 | 0.3800 | 0.8500 | 0.2675 |
| 8 | 0.3500 | 0.9714 | 0.8000 | 0.7143 |
| 9 | 0.7500 | 0.9574 | 0.9500 | 0.8155 |
| 10 | 0.1500 | 0.8363 | 0.4000 | 0.9727 |

## Appendix D. Details for the convergence study in Benchmark 3

Detailed numbers for the convergence studies carried out in Section 4.3 are provided by means of tables for the errors in matrix and fracture, analogously to Appendix A.

### *D1. Flow from top to bottom*

| **Method** | $n_{m,0}$ | $err_{m,0}$ | $n_{m,1}$ | $err_{m,1}$ | $eoc_{m,1}$ | $n_{m,2}$ | $err_{m,2}$ | $eoc_{m,2}$ |
|---|---|---|---|---|---|---|---|---|
| Box | 2664 | 4.9e−02 | 10,656 | 5.0e−02 | −0.03 | 42,624 | 5.0e−02 | 0.00 |
| TPFA | 1332 | 2.7e−02 | 4650 | 2.4e−02 | 0.19 | 17,690 | 2.4e−02 | 0.00 |
| TPFA* | 1332 | 1.3e−02 | 4650 | 6.3e−03 | 1.16 | 17,690 | 3.2e−03 | 1.01 |
| MPFA | 1332 | 2.5e−02 | 4650 | 2.4e−02 | 0.07 | 17,690 | 2.3e−02 | 0.06 |
| EDFM | – | – | – | – | – | – | – | – |
| Flux-Mortar | 1230 | 1.0e−02 | 4920 | 5.2e−03 | 0.94 | 19,680 | 2.6e−03 | 1.00 |
| P-XFEM | – | – | – | – | – | – | – | – |
| D-XFEM | 1922 | 1.9e−02 | 7442 | 1.3e−02 | 0.56 | 29,282 | 1.1e−02 | 0.24 |

| **Method** | $n_{f,0}$ | $err_{f,0}$ | $n_{f,1}$ | $err_{f,1}$ | $eoc_{f,1}$ | $n_{f,2}$ | $err_{f,2}$ | $eoc_{f,2}$ |
|---|---|---|---|---|---|---|---|---|
| Box | 152 | 3.4e−02 | 292 | 3.5e−02 | −0.04 | 576 | 3.6e−02 | −0.04 |
| TPFA | 88 | 2.9e−02 | 166 | 2.7e−02 | 0.11 | 332 | 2.7e−02 | 0.00 |

| | | | | | | | | |
|---|---|---|---|---|---|---|---|---|
| TPFA* | 93 | 1.1e−02 | 171 | 6.7e−03 | 0.81 | 337 | 5.1e−03 | 0.40 |
| MPFA | 88 | 2.8e−02 | 166 | 2.7e−02 | 0.06 | 332 | 2.7e−02 | 0.00 |
| EDFM | – | – | – | – | – | – | – | – |
| Flux-Mortar | 89 | 8.2e−03 | 178 | 5.6e−03 | 0.55 | 356 | 4.5e−03 | 0.32 |
| P-XFEM | – | – | – | – | – | – | – | – |
| D-XFEM | 199 | 3.0e−02 | 388 | 2.0e−02 | 0.61 | 769 | 1.7e−02 | 0.24 |

*D2. Flow from left to right*

| **Method** | $n_{m,0}$ | $err_{m,0}$ | $n_{m,1}$ | $err_{m,1}$ | $eoc_{m,1}$ | $n_{m,2}$ | $err_{m,2}$ | $eoc_{m,2}$ |
|---|---|---|---|---|---|---|---|---|
| Box | 2664 | 7.4e−02 | 10,656 | 7.6e−02 | −0.04 | 42,624 | 7.7e−02 | −0.02 |
| TPFA | 1332 | 5.1e−02 | 4650 | 5.3e−02 | −0.06 | 17,690 | 5.4e−02 | −0.03 |
| TPFA* | 1332 | 1.3e−02 | 4650 | 8.6e−03 | 0.66 | 17,690 | 3.6e−03 | 1.30 |
| MPFA | 1332 | 5.1e−02 | 4650 | 5.2e−02 | −0.03 | 17,690 | 5.3e−02 | −0.03 |
| EDFM | – | – | – | – | – | – | – | – |
| Flux-Mortar | 1230 | 1.4e−02 | 4920 | 8.0e−03 | 0.81 | 19,680 | 4.9e−03 | 0.71 |
| P-XFEM | – | – | – | – | – | – | – | – |
| D-XFEM | 1922 | 2.0e−02 | 7442 | 2.3e−02 | −0.21 | 29,282 | 2.3e−02 | 0.00 |

| **Method** | $n_{f,0}$ | $err_{f,0}$ | $n_{f,1}$ | $err_{f,1}$ | $eoc_{f,1}$ | $n_{f,2}$ | $err_{f,2}$ | $eoc_{f,2}$ |
|---|---|---|---|---|---|---|---|---|
| Box | 152 | 6.3e−02 | 292 | 6.7e−02 | −0.09 | 576 | 6.9e−02 | −0.04 |
| TPFA | 88 | 6.7e−02 | 166 | 6.8e−02 | −0.02 | 332 | 6.9e−02 | −0.02 |
| TPFA* | 93 | 1.2e−02 | 171 | 9.8e−03 | 0.33 | 337 | 7.2e−03 | 0.45 |
| MPFA | 88 | 6.7e−02 | 166 | 6.8e−02 | −0.02 | 332 | 6.8e−02 | 0.00 |
| EDFM | – | – | – | – | – | – | – | – |
| Flux-Mortar | 89 | 1.3e−02 | 178 | 9.6e−03 | 0.44 | 356 | 7.9e−03 | 0.28 |
| P-XFEM | – | – | – | – | – | – | – | – |
| D-XFEM | 199 | 4.3e−02 | 388 | 3.8e−02 | 0.19 | 769 | 3.8e−02 | 0.00 |

## References


Aavatsmark, I., 2002. An introduction to multipoint flux approximations for quadrilateral grids. Computat. Geosci. 6 (3), 405–432.

Ahmed, R., Edwards, M.G., Lamine, S., Huisman, B.A., Pal, M., 2015. Control-volume distributed multi-point flux approximation coupled with a lower-dimensional fracture model. J. Comput. Phys. 284, 462–489.

de Araujo Cavalcante Filho, J.S., Shakiba, M., Moinfar, A., Sepehrnoori, K., 2015. Implementation of a preprocessor for embedded discrete fracture modeling in an IMPEC compositional reservoir simulator. SPE Reservoir Simulation Symposium, 23–25 February, Houston, Texas, USA. Society of Petroleum Engineershttp://dx.doi.org/10.2118/173289-MS.

Bastian, P., Blatt, M., Dedner, A., Engwer, C., Klöfkorn, R., Kornhuber, R., Ohlberger, M., Sander, O., 2008. A generic grid interface for parallel and adaptive scientific computing. part II: implementation and tests in DUNE. Computing 82 (2–3), 121–138.

Bastian, P., Heimann, F., Marnach, S., 2010. Generic implementation of finite element methods in the distributed and unified numerics environment (DUNE). Kybernetika 46 (2), 294–315.

Berkowitz, B., 2002. Characterizing flow and transport in fractured geological media: a review. Adv. Water Resour. 25 (8–12), 861–884.

Bogdanov, I., Mourzenko, V., Thovert, J.-F., Adler, P., 2003. Two-phase flow through fractured porous media. Phys. Rev. E 68 (2), 026703.

Boon, W. M., Nordbotten, J. M., Yotov, I., 2016. Robust discretization of flow in fractured porous media. ArXiv:1601.06977 [math.NA].

Brenner, K., Groza, M., Guichard, C., Lebeau, G., Masson, R., 2016. Gradient discretization of hybrid dimensional darcy flows in fractured porous media. Numerische Mathematik 134 (3), 569–609.

Brenner, K., Hennicker, J., Masson, R., Samier, P., 2017. Gradient discretization of hybrid-dimensional darcy flow in fractured porous media with discontinuous pressures at matrixfracture interfaces. IMA J. Numer. Anal. 37 (3), 1551–1585. http://dx.doi.org/10.1093/imanum/drw044.

Brezzi, F., Lipnikov, K., Simoncini, V., 2005. A family of mimetic finite difference methods on polygonal and polyhedral meshes. Math. Mod. Meth. Appl. S. 15 (10), 1533–1551.

Caers, J., 2013. A special issue on benchmark problems, datasets and methodologies for the computational geosciences. Comput. Geosci. 50, 1–3. http://dx.doi.org/10.1016/j.cageo.2012.11.001.

Class, H., Ebigbo, A., Helmig, R., Dahle, H.K., Nordbotten, J.M., Celia, M.A., Audigane, P., Darcis, M., Ennis-King, J., Fan, Y., Flemisch, B., Gasda, S.E., Jin, M., Krug, S., Labregere, D., Naderi Beni, A., Pawar, R.J., Sbai, A., Thomas, S.G., Trenty, L., Wei, L., 2009. A benchmark study on problems related to CO2 storage in geologic formations: summary and discussion of the results. Computat. Geosci. 13 (4), 409–434.

D'Angelo, C., Scotti, A., 2012. A mixed finite element method for darcy flow in fractured porous media with non-matching grids. ESAIM: Math. Modell. Numer. Anal. 46 (2), 465–489.

De Dreuzy, J.-R., Pichot, G., Poirriez, B., Erhel, J., 2013. Synthetic benchmark for modeling flow in 3d fractured media. Comput. Geosci. 50, 59–71.

Dietrich, P., Helmig, R., Sauter, M., Hötzl, H., Köngeter, J., Teutsch, G., 2005. Flow and Transport in Fractured Porous Media. Springer.

Eymard, R., Gallouët, T., Herbin, R., 2000. Finite Volume Methods. In: Ciarlet, P.G., Lions, J.L. (Eds.), Solution of Equation in $\mathscr{R}^n$ (Part 3), Techniques of Scientific Computing (Part 3). Handbook of Numerical Analysis 7. Elsevier, pp. 713–1018. http://dx.doi.org/10.1016/S1570-8659(00)07005-8.

Firoozabadi, A., Monteagudo, J.E.P., 2004. Control-volume method for numerical simulation of two-phase immiscible flow in two- and three-dimensional discrete-fractured media. Water Resour. Res. 40, W07405. http://dx.doi.org/10.1029/2003WR002996.

Flauraud, E., Nataf, F., Faille, I., Masson, R., 2003. Domain decomposition for an asymptotic geological fault modeling. Comptes Rendus Mécanique 331 (12), 849–855.

Flemisch, B., Darcis, M., Erbertseder, K., Faigle, B., Lauser, A., Mosthaf, K., Müthing, S., Nuske, P., Tatomir, A., Wolff, M., Helmig, R., 2011. DuMu$^x$: DUNE for multi-{phase, component, scale, physics, ...} flow and transport in porous media. Adv. Water Resour. 34 (9), 1102–1112. http://dx.doi.org/10.1016/j.advwatres.2011.03.007.

Flemisch, B., Fumagalli, A., Scotti, A., 2016. A review of the xfem-based approximation of flow in fractured porous media. In: Ventura, G., Benvenuti, E. (Eds.), Advances in Discretization Methods: Discontinuities, Virtual Elements, Fictitious Domain Methods. Springer International Publishing, Cham, pp. 47–76. http://dx.doi.org/10.1007/978-3-319-41246-7_3.

Flemisch, B., Helmig, R., 2008. Numerical investigation of a mimetic finite difference method. In: Eymard, R., Hérard, J. (Eds.), Finite Volumes for Complex Applications V – Problems and Perspectives. Wiley - VCH, pp. 815–824.

Formaggia, L., Fumagalli, A., Scotti, A., Ruffo, P., 2014. A reduced model for Darcy's problem in networks of fractures. ESAIM: Math. Modell. Numer. Analysis 48, 1089–1116. http://dx.doi.org/10.1051/m2an/2013132.

Frih, N., Martin, V., Roberts, J.E., Saâda, A., 2012. Modeling fractures as interfaces with nonmatching grids. Computat. Geosci. 16 (4), 1043–1060.

Fumagalli, A., Pasquale, L., Zonca, S., Micheletti, S., 2016. An upscaling procedure for fractured reservoirs with embedded grids. Water Resour. Res. 52 (8), 6506–6525. http://dx.doi.org/10.1002/2015WR017729.

Fumagalli, A., Scotti, A., 2014. An efficient XFEM approximation of Darcy flows in fractured porous media. Oil Gas Sci. Technol. - Revue d'IFP Energies Nouvelles 69.4, 555–564.

Gassiat, C., Gleeson, T., Lefebvre, R., McKenzie, J., 2013. Hydraulic fracturing in faulted sedimentary basins: numerical simulation of potential contamination of shallow aquifers over long time scales. Water Resour. Res. 49 (12), 8310–8327. http://dx.doi.org/10.1002/2013WR014287.

Geiger, S., Dentz, M., Neuweiler, I., 2013. A novel multi-rate dual-porosity model for improved simulation of fractured and multiporosity reservoirs. SPE J. 18 (4), 670–684.

Hajibeygi, H., Karvounis, D., Jenny, P., 2011. A hierarchical fracture model for the iterative multiscale finite volume method. J. Comput. Phys. 230 (24), 8729–8743.

Hansbo, A., Hansbo, P., 2002. An unfitted finite element method, based on Nitsche's method, for elliptic interface problems. Comput. Methods Appl. Mech. Eng. 191 (47–48), 5537–5552.

Helmig, R., 1997. Multiphase Flow and Transport Processes in the Subsurface: A Contribution to the Modeling of Hydrosystems, 1 ed. Springer.

Hoteit, H., Firoozabadi, A., 2008. Numerical modeling of two-phase flow in heterogeneous permeable media with different capillarity pressures. Adv. Water Resour. 31 (1), 56–73.

Huang, H., Long, T.A., Wan, J., Brown, W.P., 2011. On the use of enriched finite element method to model subsurface features in porous media flow problems. Computat. Geosci. 15 (4), 721–736.

Karimi-Fard, M., Durlofsky, L.J., Aziz, K., 2004. An efficient discrete-fracture model applicable for general-purpose reservoir simulators. SPE J. 9 (2), 227–236.

Kolditz, O., Shao, H., Wang, W., Bauer, S., 2015. Thermo-Hydro-Mechanical-Chemical Processes in Fractured Porous Media: Modelling and Benchmarking. Springer.

Li, L., Lee, S.H., 2008. Efficient field-scale simulation of black oil in a naturally fractured reservoir through discrete fracture networks and homogenized media. SPE Reservoir Eval. Eng 11, 750–758. http://dx.doi.org/10.2118/103901-PA.

Lie, K.-A., Krogstad, S., Ligaarden, I.S., J. R. Natvig, H.M.N., Skaflestad, B., 2012. Open source matlab implementation of consistent discretisations on complex grids. Computat. Geosci. 16 (2), 297–322.

Logg, A., Mardal, K.-A., Wells, G.N., et al., 2012. Automated Solution of Differential Equations by the Finite Element Method. Springerhttp://dx.doi.org/10.1007/978-3-642-23099-8.

Martin, V., Jaffré, J., Roberts, J.E., 2005. Modeling fractures and barriers as interfaces for flow in porous media. SIAM J. Sci. Comput. 26 (5), 1667–1691.

Moinfar, A., Narr, W., Hui, M.-H., Mallison, B.T., Lee, S.H., 2011. Comparison of discrete-fracture and dual-permeability models for multiphase flow in naturally fractured reservoirs. SPE Reservoir Simulation Symposium. Society of Petroleum Engineers.

Moinfar, A., Varavei, A., Sepehrnoori, K., Johns, R.T., 2014. Development of an efficient embedded discrete fracture model for 3d compositional reservoir simulation in fractured reservoirs. SPE J. 19 (2), 289–303.

Müthing, S., 2015. A Flexible Framework for Multi Physics and Multi Domain PDE Simulations. University of Stuttgart Ph.D. thesis.

Neumann, S.P., 2005. Trends, prospects and challenges in quantifying flow and transport through fractured rocks. Hydrogeol. J. 13, 124–147.

Nordbotten, J., Flemisch, B., Gasda, S., Nilsen, H., Fan, Y., Pickup, G., Wiese, B., Celia, M., Dahle, H., Eigestad, G., Pruess, K., 2012. Uncertainties in practical simulation of CO2 storage. Int. J. Greenhouse Gas Control 9, 234–242. http://dx.doi.org/10.1016/j.ijggc.2012.03.007.

Panfili, P., Cominelli, A., 2014. Simulation of miscible gas injection in a fractured carbonate reservoir using an embedded discrete fracture model. Abu Dhabi International Petroleum Exhibition and Conference, 10–13 November, Abu Dhabi, UAE. Society of Petroleum Engineershttp://dx.doi.org/10.2118/171830-MS.

Panfili, P., Cominelli, A., Scotti, A., 2013. Using Embedded Discrete Fracture Models (EDFMs) to simulate realistic fluid flow problems. Second EAGE Workshop on Naturally Fractured Reservoirs, Muscat, Oman.

Pfunt, H., Houben, G., Himmelsbach, T., 2016. Numerical modeling of fracking fluid migration through fault zones and fractures in the north german basin. Hydrogeol. J. 24 (6), 1343–1358. http://dx.doi.org/10.1007/s10040-016-1418-7.

Reichenberger, V., Jakobs, H., Bastian, P., Helmig, R., 2006. A mixed-dimensional finite volume method for two-phase flow in fractured porous media. Adv. Water Resour. 29 (7), 1020–1036. http://dx.doi.org/10.1016/j.advwatres.2005.09.001.

Sahimi, M., 2011. Flow and Transport in Porous Media and Fractured Rock: From Classical Methods to Modern Approaches. John Wiley & Sons.

Sandve, T.H., Berre, I., Nordbotten, J.M., 2012. An efficient multi-point flux approximation method for discrete fracture-matrix simulations. J. Comput. Phys. 231 (9), 3784–3800. http://dx.doi.org/10.1016/j.jcp.2012.01.023.

Schwenck, N., 2015. An XFEM-Based Model for Fluid Flow in Fractured Porous Media. University of Stuttgart Ph.D. thesis.

Schwenck, N., Flemisch, B., Helmig, R., Wohlmuth, B., 2015. Dimensionally reduced flow models in fractured porous media: crossings and boundaries. Computat. Geosci. 19 (6), 1219–1230. http://dx.doi.org/10.1007/s10596-015-9536-1.

Singhal, B.B.S., Gupta, R.P., 2010. Applied Hydrogeology of Fractured Rocks. Springer Science & Business Media.

Swedish Nuclear Power Inspectorate (SKI), 1987. The International Hydrocoin Project–Background and Results. Paris, France: Organization for Economic Co-operation and Development.

Taherdangkoo, R., Tatomir, A., Taylor, R., Sauter, M., 2017. Numerical investigations of upward migration of fracking fluid along a fault zone during and after stimulation. Energy Procedia 125, 126–135. http://dx.doi.org/10.1016/j.egypro.2017.08.093.

Tatomir, A.-B., 2012. From Discrete to Continuum Concepts of Flow in Fractured Porous Media. Ph.D. thesis. University of Stuttgart.

Tene, M., Bosma, S.B., Kobaisi, M.S.A., Hajibeygi, H., 2017. Projection-based embedded discrete fracture model (pEDFM). Adv. Water Resour. 105, 205–216. http://dx.doi.org/10.1016/j.advwatres.2017.05.009.

Tunc, X., Faille, I., Gallouët, T., Cacas, M.C., Havé, P., 2012. A model for conductive faults with non-matching grids. Computat. Geosci. 16 (2), 277–296.